

**Polytechnic University of Turin**

---

DEPARTMENT OF MECHANICAL AND AEROSPACE ENGINEERING

Master of Science in Aerospace Engineering

MASTER'S DEGREE THESIS



# Study of turbomachinery flow using Large-Eddy Simulation

Thesis Advisor:

**Prof. Francesco LAROCCA**

Candidate:

**Kristi SHTEMBARI**

Assistent Supervisor:

**Prof. Andrea FERRERO**

---

Academic Year 2019–2020

Kristi Shtembari: *Study of turbomachinery flow using Large-Eddy Simulation* |  
Master's Degree thesis in Aerospace Engineering, Polytechnic University of Turin.  
© Copyright December 2020.

Computational resources were provided by HPC@POLITO, which is a project of  
Academic Computing within the Department of Control and Computer Engineering  
at the Polytechnic University of Turin.

---

Polytechnic University of Turin:

[www.polito.it](http://www.polito.it)

Department of Mechanical and Aerospace Engineering:

[www.dimeas.polito.it](http://www.dimeas.polito.it)

HPC@POLITO:

[www.hpc.polito.it](http://www.hpc.polito.it)

*To my family,  
for always being on my side*

# Abstract

The present thesis is dedicated to the study of turbulent flows inside an aeronautical engine turbine by means of Large-Eddy Simulation (LES). For many decades, the turbomachinery flow has been one of the main focuses of research in Computational Fluid Dynamics (CFD). The significant developments achieved in aero-engine performances are strictly connected to different complex geometries and flow configurations being employed. Thus, there is a greater need for high fidelity simulations to be performed in order to reach an acceptable level of accuracy and quality in the design and optimization processes of such flows, since the use of large scale test facilities can be very expensive and disadvantageous.

Due to the reduced computational cost with reference to Direct Numerical Simulation (DNS) and the much higher accuracy if compared to Reynolds-Averaged Navier-Stokes (RANS) models, the LES approach has become a very powerful analysis tool in many engineering fields nowadays. Even though many issues have not been addressed yet, the LES approach has proven its effectiveness in complex geometries and flow configurations such as low pressure turbine or gas turbine combustor flows.

In the current work, a first introduction to different types of simulations for turbulent flows is provided. Afterwards, emphasis is placed on the LES approach formalism and Sub-Grid Scale (SGS) closure models. An existing code based on a Discontinuous-Galerkin finite element method is used to conduct a LES on the T106A rotor passage blade cascade of a low pressure turbine. The impact of the adopted physical model and discretization scheme on some of the variables of interest is therefore analyzed. Finally, the achieved numerical results are compared to experimental data and other numerical work present in literature. One of the main goals of this work is to retrieve high accuracy data of the flow field in the whole computational domain, in order that such data could eventually be used in future work to improve existing RANS models by means of Machine Learning techniques.

**Keywords:** turbomachinery flow, Large-Eddy Simulation (LES), Sub-Grid Scale (SGS) modeling, Discontinuous-Galerkin finite element method, T106A.

# Sommario

La presente attività di tesi è indirizzata allo studio dei flussi turbolenti all'interno di una turbina aeronautica mediante una simulazione di tipo Large-Eddy Simulation (LES). Negli ultimi decenni, il flusso nelle turbomacchine è stato uno degli argomenti principali della ricerca nel campo della Fluidodinamica Computazionale (CFD). Il notevole sviluppo ottenuto nelle prestazioni dei motori per aeromobili è strettamente legato all'impiego di geometrie e configurazioni di flusso complesse. Pertanto, sono necessarie simulazioni di elevata affidabilità al fine di ottenere un livello accettabile di accuratezza e di qualità dei processi di progettazione e di ottimizzazione delle turbomacchine impiegate nel campo aeronautico, in quanto l'utilizzo di grandi strutture di prova risulta essere molto costoso e svantaggioso.

In virtù del ridotto costo computazionale rispetto alle simulazioni di tipo Direct Numerical Simulation (DNS) e della maggiore accuratezza nei confronti dei modelli di tipo Reynolds-Averaged Navier-Stokes (RANS), l'approccio LES è diventato uno strumento di analisi altamente efficace in diversi campi ingegneristici. Sebbene molte problematiche riguardanti le LES non sono ancora state affrontate, tale approccio ha dimostrato la sua efficienza in diverse geometrie e configurazioni di flusso complesse, come i flussi all'interno delle turbine di bassa pressione e dei combustori delle turbine a gas.

Nel presente lavoro, vengono inizialmente introdotte alcune delle tipologie principali di simulazioni per i flussi turbolenti. In seguito, l'enfasi è posta sulla teoria dell'approccio LES e sui modelli di chiusura dei termini Sub-Grid Scale (SGS). Un codice esistente basato sul metodo Galerkin-Discontinuo agli elementi finiti viene utilizzato per effettuare una LES sulla schiera di pale rotoriche T106A di una turbina di bassa pressione. Viene quindi analizzata l'influenza del modello fisico e del metodo di discretizzazione adottati su alcune grandezze di interesse. Infine, i risultati numerici ottenuti mediante il codice vengono confrontati con i dati sperimentali e con altri risultati numerici disponibili in letteratura. Uno degli obiettivi principali del lavoro di tesi è quello di ottenere dei risultati molto accurati del campo di flusso nell'intero dominio computazionale, in modo da poter eventualmente utilizzare questi dati in studi futuri per migliorare dei modelli RANS esistenti mediante tecniche di Machine Learning.

**Parole chiave:** turbomacchine, Large-Eddy Simulation (LES), modelli Sub-Grid Scale (SGS), metodo Galerkin-Discontinuo agli elementi finiti, T106A.

# Acknowledgements

I would like to express my special thanks of gratitude to prof. Francesco Larocca and prof. Andrea Ferrero, who gave me the the opportunity to work on the present topic of studying turbulent turbomachinery flows by means of numerical simulations. I would like to thank them for the continuous support and for guiding me through my work. Fascinating as the argument is, it helped me a lot to make my first steps towards the field of research and broaden my knowledge on various areas of Computational Fluid Dynamics.

Secondly, I would like to thank my parents and my brother for always being of great support and for their countless love and affection. I am extremely grateful to my parents for their sacrifices in raising and educating me with the best of values, and to my brother for all of the advice and wise words he has provided me over the last several years and all of the incredible strength he has forced me to see in myself.

Lastly, I would like to thank Piero and Luigi for all the adventures they gifted me with. Thanks to them, I had the opportunity to discover Italy in a way that I will never forget. I will always hold them dear to my heart for being such marvelous and special persons in my life. And I cannot fail to remember Marie and Adrian, my best Erasmus companions who rendered the experience full of excitement and joy.

# Table of Contents

<b>List of Symbols</b>	<b>X</b>
<b>1 Introduction</b>	<b>1</b>
1.1 A general overview on LES . . . . .	6
1.2 Current work . . . . .	8
<b>2 Theoretical background</b>	<b>9</b>
2.1 Energy cascade and Kolmogorov hypotheses . . . . .	9
2.2 The Large-Eddy Simulation approach . . . . .	13
2.2.1 Governing equations . . . . .	14
2.2.2 Convolution filtering operation . . . . .	16
2.2.3 Favre filtering . . . . .	19
2.2.4 Filtered governing equations . . . . .	20
2.2.5 SGS modeling . . . . .	22
2.3 Concluding remarks . . . . .	25
<b>3 Methodology</b>	<b>27</b>
3.1 Discontinuous-Galerkin finite element method . . . . .	27
3.2 T106A test case description . . . . .	31
3.3 Mesh generation . . . . .	34
3.4 Flow and boundary conditions . . . . .	37
3.5 Parallel work . . . . .	38
<b>4 Numerical results</b>	<b>39</b>
4.1 Simulations setup . . . . .	39
4.2 Flow visualization . . . . .	42
4.3 Wake losses profile . . . . .	47
<b>5 Conclusions</b>	<b>49</b>
<b>Bibliography</b>	<b>55</b>
<b>List of Abbreviations</b>	<b>56</b>

# List of Figures

1.1	Use of CFD in turbomachinery flows (Gerretsen and Kurz, 2009). . . . .	1
1.2	Three-dimensional view of the aft region of the suction surface of the blade, showing isosurfaces of instantaneous spanwise vorticity (Garai et al., 2015). . . . .	2
1.3	Commercial aircraft engine flight envelope and the associated LPT operating range Reynolds number (Hourmouziadis, 1989). . . . .	3
1.4	Turbine cascade performances with different flow typologies (Hourmouziadis, 1989). . . . .	4
1.5	Instantaneous velocity magnitude for: DNS (top) and LES (bottom) (de Wiart and Hillewaert, 2012). . . . .	5
1.6	Comparison between different types of simulation approaches for turbulent flows (Deck et al., 2014). . . . .	6
1.7	LES hierarchy indicating the importance of each element (Tyacke and Tucker, 2015). . . . .	7
2.1	Schematic representation of the energy cascade in a fully turbulent flow at high Reynolds number (Pope, 2001). . . . .	11
2.2	Energy spectrum for homogeneous turbulence (Kalmár-Nagy and Bak, 2019). . . . .	12
2.3	Comparison between different simulation approaches for turbulent flows according to the scales of eddies resolved within the model (Pope, 2001). . . . .	14
2.4	Gaussian, cutoff and box filters plotted for the same filter width (cutoff wavenumber): (a) in physical space and (b) in wavenumber space (Stoll, 2014). . . . .	18
2.5	Box filter applied to the velocity component in physical space in a one-dimensional case (Fröhlich and Rodi, 2002). . . . .	18
2.6	Comparison between different filters applied to the energy spectrum in case of homogeneous and isotropic turbulence (Laval, 2020). . . . .	19
2.7	Representation of different scale subranges in LES for homogeneous and isotropic turbulence (Maulik and San, 2018). . . . .	23
3.1	Dissipation relation of Discontinuous-Galerkin spectral element methods with Gauss nodes, from $N = 1$ to $N = 10$ . $K^* = \frac{K}{N+1}$ is the normalized wavenumber and $\Omega^*$ is the corresponding modified normalized wavenumber (Gassner and Kopriva, 2011). . . . .	31

3.2	High-Speed Cascade Wind Tunnel of the Universität der Bundeswehr München (Stadt Müller et al., 2000). . . . .	32
3.3	T106A blade airfoil geometry (Michelassi et al., 2015). . . . .	33
3.4	2D mesh generated with Gmsh. . . . .	35
3.5	3D mesh generated with Gmsh. . . . .	36
3.6	Imposed boundary conditions for numerical computation. . . . .	37
4.1	Force coefficients evolution over time for second order simulation: Instantaneous values on the left and mean values on the right. The red line denotes the separation between discarded convective times and those used for the averaging process of the data. . . . .	40
4.2	Force coefficients evolution over time for third order simulation: Instantaneous values on the left and mean values on the right. The red line denotes the separation between discarded convective times and those used for the averaging process of the data. . . . .	41
4.3	Instantaneous Mach field visualizations at the midspan section for: (a) second order simulation and (b) third order simulation. Instantaneous velocity magnitude field at the midspan section for (c) reference DNS (Garai et al., 2015). . . . .	43
4.4	Instantaneous spanwise vorticity fields at the midspan section for: (a) second order simulation, (b) third order simulation and (c) reference DNS (Garai et al., 2015). . . . .	44
4.5	Isosurfaces of instantaneous second invariant of the velocity gradient tensor (Q-criterion) for: (a) second order simulation and (b) third order simulation. . . . .	45
4.6	Isosurfaces of instantaneous entropy field for: (a) second order simulation and (b) third order simulation. . . . .	46
4.7	Wake measurement plane. . . . .	47
4.8	Wake loss coefficient profile for second and third order simulations, compared to experimental data (Stadt Müller et al., 2000) and reference DNS (Garai et al., 2015). The values refer to time- and spanwise-averaged total pressure losses in the wake, measured on a plane $40\%C$ downstream from the cascade exit. . . . .	48

# List of Tables

3.1	Parameters defining the T106A test case configuration . . . . .	34
-----	---	----

# List of Symbols

$\overline{(\cdot)}$	Convolution filtering operator
$\widehat{(\cdot)}$	Fourier transform operator
$\langle(\cdot)\rangle$	Reynolds averaging operator
$\widetilde{(\cdot)}$	Favre filtering operator
$\dot{(\cdot)}$	Computable quantities
$d_m/C$	Wake measurement plane position
$h/C$	Aspect ratio
$t/C$	Pitch-to-chord ratio
$C$	Chord length
$C$	Kolmogorov universal constant
$C_{ax}$	Axial chord length
$C_{F_{x_i}}$	Coefficients of the force components on the blade
$C_p$	Specific heat at constant pressure
$C_s$	Smagorinsky constant
$C_v$	Specific heat at constant volume
$E$	Total energy per mass unit
$E(k)$	Energy spectrum
$E_{ref}$	Reference total energy per mass unit
$\mathbf{F}$	Flux vector field
$\mathbf{F}_h^*$	Numerical flux vector field at the element's boundary
$G$	Kernel filter function
$\mathbf{G}$	Convective flux vector field
$h_g$	Mesh extension along the spanwise direction
$\mathbf{H}$	Diffusive flux vector field
$k$	Wavenumber
$\mathbf{k}$	Wavenumber vector
$k_c$	Cutoff wavenumber
$l$	Characteristic length of eddies in the inertial subrange
$l_0$	Characteristic length of large eddies
$L_{ref}$	Reference length
$M$	Mach number
$[\mathbf{M}]$	Element mass matrix
$M_{2,is}$	Exit isentropic Mach number
$\hat{\mathbf{n}}$	Outward-pointing unity vector at the element's boundary
$N$	Number of isosurfaces levels
$N_e$	Number of elements of the computational domain

$p$	Static pressure
$p_2$	Static pressure at the outlet
$p_{ref}$	Reference pressure
$p_t$	Total pressure
$p_{t1}$	Total pressure at the inlet
$P^p$	Space of polynomials of degree up to $p$
$Pr$	Prandtl number
$q$	Velocity magnitude
$q_{2,is}$	Exit isentropic velocity
$q_j$	Heat flux
$q_{ref}$	Reference velocity
$Q - criterion$	Second invariant of the velocity gradient tensor
$R$	Gas constant
$\mathbf{R}(\tilde{\mathbf{U}})$	Numerical flux term
$Re$	Reynolds number
$Re_0$	Reynolds number of large eddies
$Re_{2,is}$	Exit isentropic Reynolds number
$Re_{ref}$	Reference Reynolds number
$s$	Entropy
$s_{ref}$	Reference entropy
$S_{ij}$	Rate-of-strain tensor
$ \tilde{S}_{ij} $	Computable rate-of-strain tensor characteristic
$t$	Time
$t$	Blade cascade pitch
$t_c$	Convective time
$t_{ref}$	Reference time
$T$	Static temperature
$T_E$	Energy transfer rate from large to small eddies
$T_h$	Ensemble of the computational domain elements
$T(l)$	Energy transfer rate in the inertial subrange
$T_{ref}$	Reference temperature
$T_t$	Total temperature
$T_{t1}$	Total temperature at the inlet
$u_0$	Characteristic velocity of large eddies
$u_i$	Velocity components
$u_\eta$	Kolmogorov velocity scale
$U$	Conservative variables vector
$\tilde{\mathbf{U}}$	Vector of the discrete approximated conservative variables
$U_h$	Approximate function of the conservative variables
$\tilde{U}_i$	Discrete values of the approximated conservative variables
$v$	Test function
$V_h$	Discrete functional space
$\mathbf{x}$	Position vector
$x_i$	Cartesian coordinates
$y^*$	Normalized pitchwise coordinate

$\mathcal{D}_j$	SGS viscous diffusion
$\mathcal{J}_j$	SGS turbulent diffusion
$\mathcal{L}$	Characteristic length of the flow
$\mathcal{Q}_j$	SGS temperature flux
$\mathcal{T}$	Characteristic time of the flow
$\mathcal{U}$	Characteristic velocity of the flow
$\beta_1$	Geometric inlet angle
$\gamma$	Stagger angle
$\gamma$	Isentropic expansion factor
$\delta_{ij}$	Delta Dirac function
$\Delta$	Filter width
$\Delta_t$	Test filter width
$\epsilon$	Energy dissipation
$\eta$	Kolmogorov lengthscale
$\lambda$	Thermal conductivity
$\mu$	Dynamic viscosity
$\mu_{ref}$	Reference dynamic viscosity
$\nu$	Kinematic viscosity
$\nu_{sgs}$	Eddy-viscosity
$\xi$	Wake deficit coefficient
$\rho$	Density
$\rho_{ref}$	Reference density
$\sigma_{ij}$	Shear-stress tensor
$\tau_0$	Characteristic time of large eddies
$\tau_{ij}$	SGS stress tensor
$\tau_{ij}^d$	Deviatoric part of the SGS stress tensor
$\tau_{kk}$	Isotropic part of the SGS stress tensor
$\tau_\eta$	Kolmogorov timescale
$\phi$	Generic scalar quantity
$\phi'$	Unfiltered part of scalar quantity $\phi$
$\Phi$	Basis of the functional space $V_h$
$\Phi_i$	Basis functions
$\psi$	Generic scalar quantity
$\omega$	Frequency
$\Omega$	Computational domain
$\Omega_e$	Generic element of the computational domain
$\partial\Omega_e$	Element's boundary

# Chapter 1

## Introduction

Turbomachinery flow represents one of the most challenging fields in Computational Fluid Dynamics (CFD). If one considered turbomachines employed in aircraft propulsion, the internal flow is characterized by a stochastic and a deterministic nature, with the former being driven by the turbulence and the latter by the stator-rotor interaction (Richard D Sandberg and Michelassi, 2019). The very complex geometry, unsteadiness, secondary flows, boundary layers, transition and relaminarization regions are only some of the many other aspects to be taken into account in a gas turbine design process, making the use of large scale test facilities overly expensive and disadvantageous. Therefore, the use of CFD is compulsory in order to provide a reduction in costs, though due to the aforementioned flow complexities in turbomachines it is not always possible to obtain the required accuracy of the flow physics.

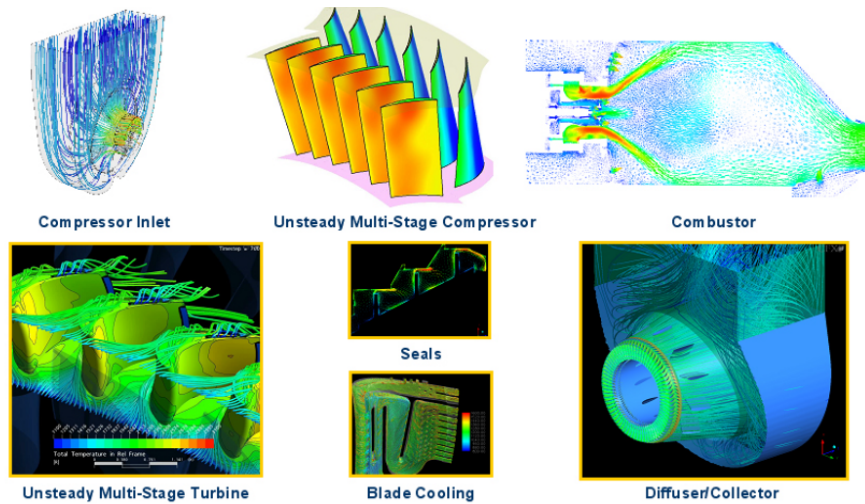


**Figure 1.1:** Use of CFD in turbomachinery flows (Gerretsen and Kurz, 2009).

The current work concentrates on the turbulent aspect of the turbomachinery flow. Generally, turbulent motion is what characterizes a large variety of flow types, from the naturally occurring ones to the practical engineering flows. The very three-dimensional, time-dependent and random nature of turbulence makes its modeling one of the most difficult problems in classical physics. Its chaotic

nature comprises a wide range of scales of motion which increases with the Reynolds number and further difficulties arise from the continuous non-linear interaction between the different scales, energetically speaking. Hence, particular attention of research in CFD has been focused on turbulent flows, with its primary reliance being the nowadays constantly growing computing power.

Over the past decades, many types of simulation and models for turbulent flows have been proposed, with the most complete and accurate approach being the Direct Numerical Simulation (DNS). The DNS simulation consists in resolving directly the Navier-Stokes equations without introducing any turbulence model. The problem must be resolved down to the smallest scales of turbulent motion, denominated as Kolmogorov scales (Pope, 2001). Since the size of Kolmogorov scales with respect to the size of the largest ones varies as  $Re^{-3/4}$ , it is obvious that the grid resolution must increase with increasing Reynolds number in order to capture even the smallest scales, with a consequent strong elevation in computational cost. This makes the application of DNS prohibitive for typical Reynolds numbers of turbomachinery flow ( $10^5 - 10^7$ ).

Nevertheless, with the current computing performances, many researchers have been able to perform DNS on a large variety of Low Pressure Turbines (LPT), where typical Reynolds numbers are relatively moderate. Garai et al., 2015 recently validated their code based on a Discontinuous-Galerkin spectral element approach on the LPT rotor passage blade cascade T106A. Their data, using simulations up to the 8<sup>th</sup> order, perfectly matched experimental results. From different flow visualizations, it can be easily noticed how even the smallest scales are captured by the DNS, as shown in Fig. 1.2.

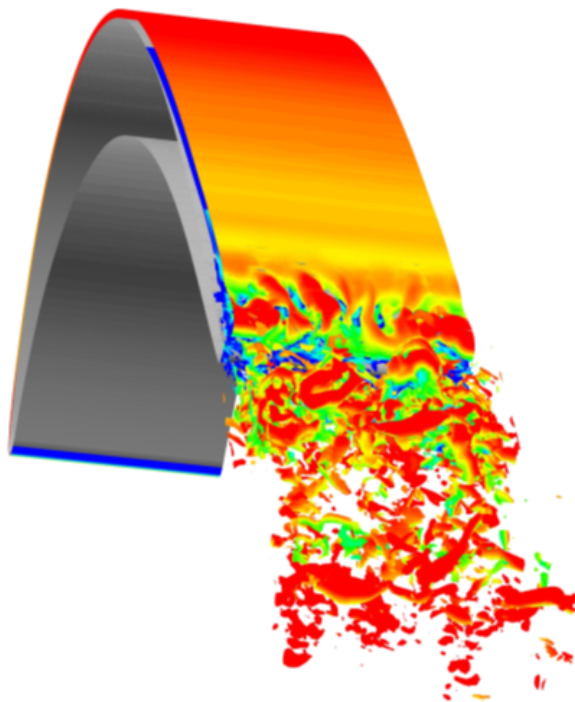


**Figure 1.2:** Three-dimensional view of the aft region of the suction surface of the blade, showing isosurfaces of instantaneous spanwise vorticity (Garai et al., 2015).

As far as flow inside a LPT is concerned, Babajee, 2013 focused his research activity on the investigation of the separation-induced transition phenomenon occurring in the latter. The main goal of his work was to reduce the losses inside the LPT by increasing its efficiency, which is strongly affected by the separation and transition phenomena. Fig. 1.3 shows how a LPT for a typical commercial aircraft covers a wide range of operating points, going from  $Re = 200000$  at cruise to  $Re = 400000$  at take-off. Nowadays, the Reynolds numbers at cruise conditions could even go below 100000.

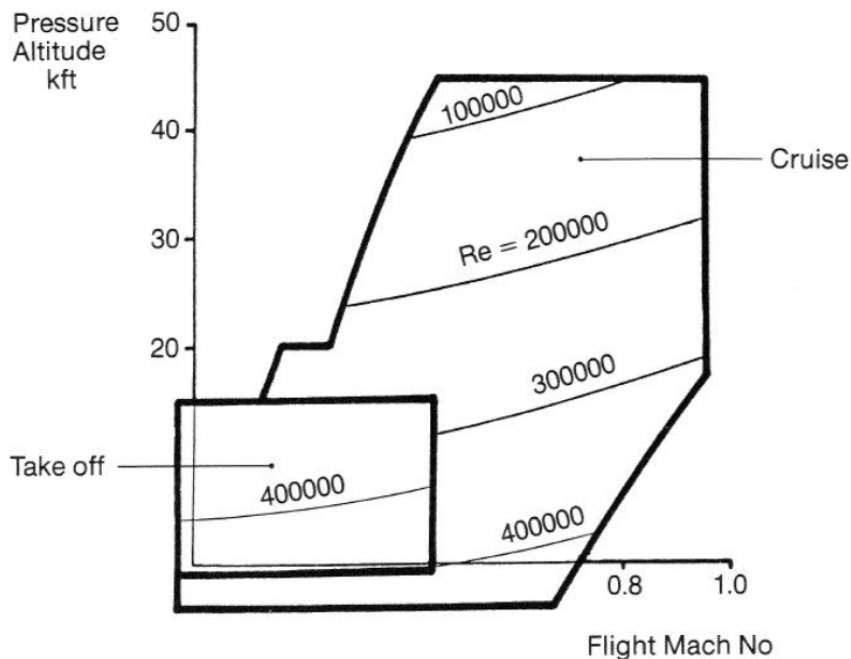


**Figure 1.3:** Commercial aircraft engine flight envelope and the associated LPT operating range Reynolds number (Hourmouziadis, 1989).

Within this wide range of operating Reynolds numbers, the changing flow conditions lead to different types of separation and transition occurring, as described in Fig. 1.4. First of all, case (a) is not really encountered in nowadays LPT. At high Reynolds numbers for case (b), the flow remains attached to the wall and follows the exit direction imposed by the blade at the trailing edge. For lower Reynolds numbers in case (c), a short separation bubble appears, that is a zone where the flow separates from the wall and reattaches further aft. It is characterized by a dead air region followed by a recirculation area. However, this type of bubble has no considerable effect on the blade losses. Case (d) illustrates the bursting of the bubble as a long separation bubble. Finally, case (e) leads to an open separation in which the flow exits the cascade according to a much smaller angle than the one imposed by the blade, therefore this action is detrimental in terms of losses. Thus, what one hopes to achieve while designing a LPT is to decrease the Reynolds number at bursting defined by case (d), by also choosing the best trade-off between high Reynolds number regime (take-off) and low Reynolds number regime (cruise).

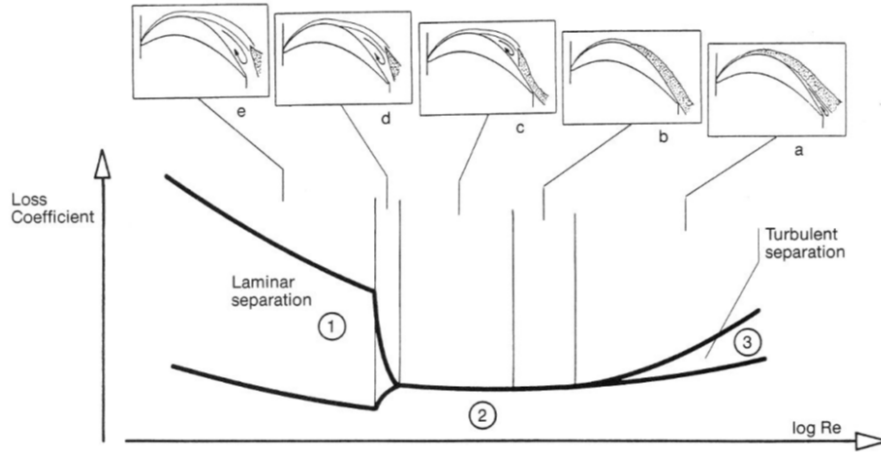


**Figure 1.4:** Turbine cascade performances with different flow typologies (Hourmouziadis, 1989).

Considering the wide range of operating Reynolds numbers to be simulated, a DNS would be computationally not affordable for this kind of investigation. Furthermore, since in most practical engineering problems the major interest resides in the mean flow quantities, such as mean lift and drag coefficients, the Reynolds-Averaged Navier-Stokes (RANS) approach is widely used. This approach is based on time-averaging (for steady problems) or ensemble-averaging (for unsteady problems) the Navier-Stokes equations and solving the averaged equations system for the mean flow properties. Residual terms arise from the averaging process, as the widely known in literature Reynolds stresses. Thus, in order to close the problem these terms need modeling. Many turbulence closure methods have been proposed, with the most diffused ones being the turbulent-viscosity model and the Reynolds Stress Model (RSM) (Pope, 2001). The RANS approach still constitutes the main design tool for many application fields due to its simplicity and very low computational cost compared to other available approaches such as DNS or LES. Nevertheless, RANS modeling fails to accurately predict regions where separation, transition or relaminarization might occur. The method's limitations reside in its strong dependence on the turbulence model choice and empirical correlations used in transitional regions which lack of universality.

Despite these drawbacks, in order to investigate the separation and transition effects on the LPT performances, Babajee, 2013 used a RANS approach based on the innovative  $\gamma - \overline{Re}_{\theta t}$  transition model. From the comparisons with the experiments, the methodology used gave predictions that were in good agreement with what was measured, therefore concluding that the method was reliable in predicting transitional flows on high lift LPT blades with mild diffusion rate. However, it turned out that for high lift LPT blades with high diffusion rate, the predictions were underestimated.

To overcome the DNS and RANS limitations an intermediate approach has been proposed, which consists in resolving explicitly the largest scales of the turbulent motion while modeling the smallest ones, hence the name Large-Eddy Simulation

(LES). This scale separation considerably reduces the computational cost of a LES compared to DNS since a more moderate grid resolution is required. Moreover, the three-dimensional, unsteady nature of the largest eddies being captured by the LES approach makes this method viable to study aero-acoustics, fluid-structure coupling or other phenomena in which large-scale unsteadiness is important and RANS models would fail to predict an accurate solution (Fröhlich and Rodi, 2002). Also, considering the smallest scales are more universal than the largest ones, their modeling shall be easier and have a lighter impact on the flow field solution accuracy, rather than modeling all scales within one method as done with RANS.

Therefore, the LES approach has been widely used for the investigation of the aforementioned transitional separated flows on LPT, generally providing satisfactory results. Not recently, de Wiart and Hillewaert, 2012 used a high order Discontinuous-Galerkin method to perform a LES on the transitional flow past the SD7003 airfoil. The very interesting dispersion and dissipation properties of the Discontinuous-Galerkin method allow for the numerical error of the method's itself to implicitly provide the necessary dissipation that accounts for the presence of the smallest unrepresented scales while resolving the flow. This kind of approach is known in literature as Implicit LES (ILES). Also, the local and discontinuous nature of the method allows it to efficiently deal with complex geometries such as LPT. The performed studies demonstrated that the numerical results obtained for the considered test case are in good agreement with the reference experimental data and the DNS simulations conducted using the same discretization scheme. It can be noticed in Fig. 1.5 how the velocity field is somehow filtered by the LES solution with reference to the DNS, with the largest scales however having been captured accurately.

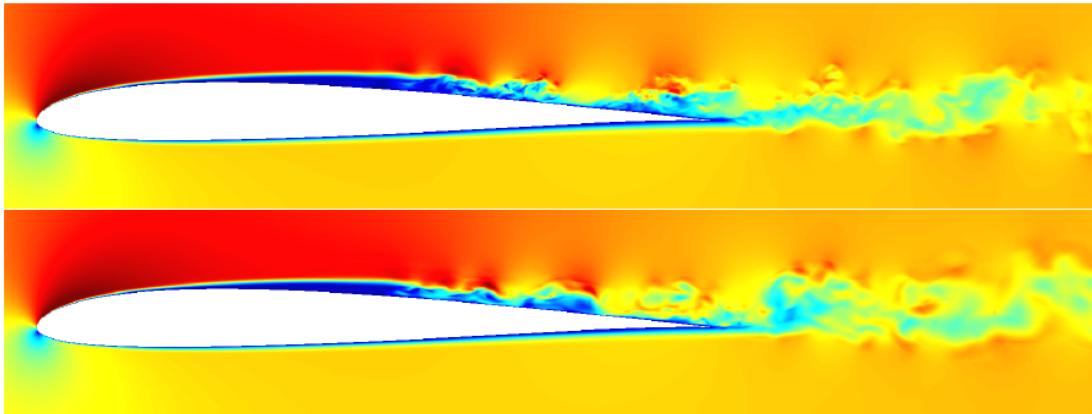


**Figure 1.5:** Instantaneous velocity magnitude for: DNS (top) and LES (bottom) (de Wiart and Hillewaert, 2012).

However though, the LES approach can be 10 to 100 times more costly than a simple RANS model. Moreover, in wall-bounded flows, the grid resolution must increase considerably while getting nearer to the solid boundaries, since in these regions even the most dominating turbulent scales become very small in size. Thus, a new approach has been proposed which relies on the idea of coupling LES and RANS

models (Jochen Fröhlich and Von Terzi, 2008). This hybrid LES/RANS approach takes advantage of the ease of implementation of RANS models and the high precision achieved by the LES approach, giving birth to computationally affordable and reliable models such as Detached-Eddy Simulation (DES) or Scale-Adaptive Simulation (SAS).

In DES for instance, near wall regions and regions where the dominant scales cannot be represented by the computational grid are assigned to the RANS mode of solution. As scales size increases, the regions are solved using the LES mode. Thus, the grid resolution is not as demanding as pure LES, thereby considerably reducing the computational cost, while maintaining an elevated level of accuracy. An interesting study using this hybrid kind of approach was performed by Piomelli and Balaras, 2002. Fig. 1.6 provides a comparison between the different simulation approaches for turbulent flows described in the current section, based on their computational cost and turbulence modeling influence.

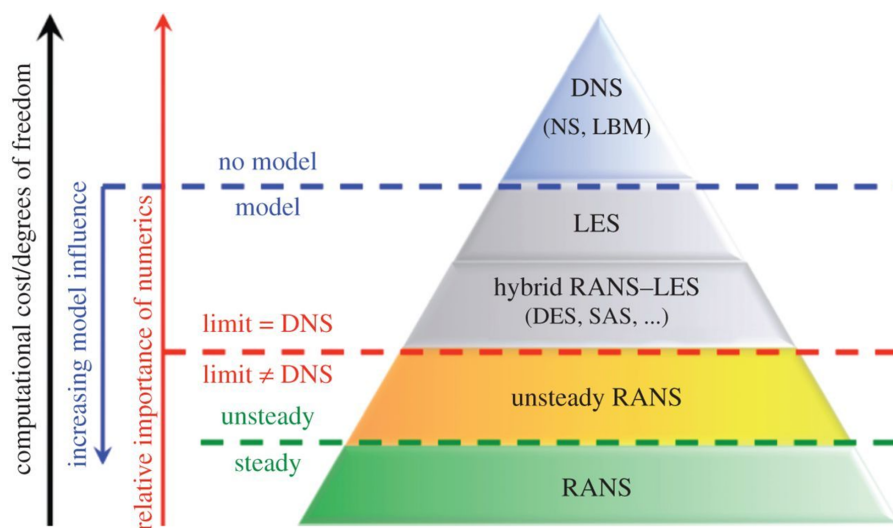


**Figure 1.6:** Comparison between different types of simulation approaches for turbulent flows (Deck et al., 2014).

## 1.1 A general overview on LES

The present work concentrates exclusively on the LES approach, therefore a general overview might be important before getting more into detail. The Large-Eddy Simulation approach was first introduced by Smagorinsky, 1963 to simulate atmospheric air current, and was first applied to engineering by Deardorff et al., 1970. But it was only after the 1990s that LES applications started to increase due to the significant improvements in computing performances and since it had already become clear that the RANS approach couldn't offer the required accuracy to capture many flow physics such as separation, transition or secondary flows.

Nowadays, with the employment of high performance computing and the considerable developments made in the LES field in the past few decades, this approach finds application in many complex engineering flows and geometries such as transitional flows over turbine blades or gas turbine combustors. The ability to perform

high fidelity simulations where the RANS approach fails and the DNS is inapplicable for its bloated computational cost has made LES a very powerful tool in the engineering field. Nevertheless, the LES approach still presents many issues and challenges to be addressed before being able to completely replace RANS models and become the main analysis tool in such field of application (Zhiyin, 2015).

One of the issues that still characterizes the LES approach is that, despite the high performances of the computing resources at present, its computational cost still is significantly high for LES to become a routine basis tool for engineering flow simulations. Also, the turbulence closure modeling for LES, alias Sub-Grid Scale (SGS) modeling, used to approximate the effects of the smallest scales of turbulent motion on the largest ones, presents another issue albeit of minor importance if compared to other challenges, such as inflow boundary conditions and wall layer modeling (Fig. 1.7). Another important aspect of the LES simulations are the compressibility effects. Up to date, most of the available models for the SGS stress tensor, inflow boundary layer or wall layer modeling have been developed for incompressible flows and have usually been directly applied to compressible fluids. Moreover, one can anticipate that the incompressible case problem consists of one continuity equation and three momentum equations, with the SGS stress tensor being the only residual term present. On the other hand, in the compressible case, the energy equation is added to the governing equations system introducing additional SGS terms. Therefore, the case of compressible flows problem is much more complex since more terms need modeling (Garnier et al., 2009).

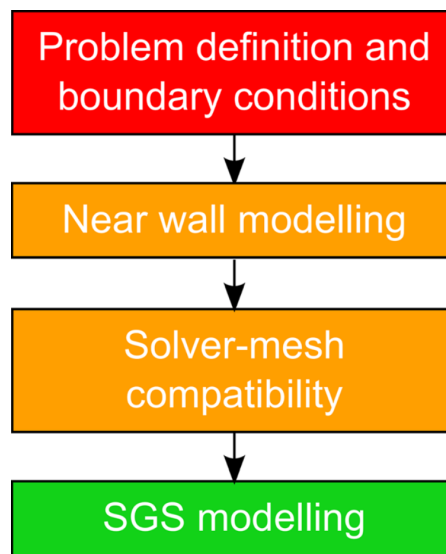


**Figure 1.7:** LES hierarchy indicating the importance of each element (Tyacke and Tucker, 2015).

However, with the enormous efforts into improving the current LES performances and the ever increasing computing power, in the years to come, LES will become always a more powerful analysis tool, though many challenges still have to be overcome before LES totally replaces RANS in the engineering field.

## 1.2 Current work

As anticipated in the previous section, the current study focuses on the LES approach applied to turbomachinery flow. To this purpose, a research code based on a Discontinuous-Galerkin finite element method, developed in the Department of Mechanical and Aerospace Engineering (DIMEAS) by Ferrero, 2015, is used to perform a LES on the T106A rotor passage cascade blade of a LPT. The document's structure is organized as follows:

- Chapter 2:** A first insight in the LES formalism for compressible flows is provided. The filtering operation is introduced along with the filtered governing equations, followed by a brief description of the current state-of-the-art of SGS modeling.
- Chapter 3:** The Discontinuous-Galerkin finite element method is described briefly, along with the T106A test case configuration and numerical setup.
- Chapter 4:** Numerical results are reported and compared to the experimental data and other numerical work present in literature.
- Chapter 5:** Conclusions on the achieved results are presented.

# Chapter 2

## Theoretical background

As stated in the previous chapter, the nature of the turbulent motion is three-dimensional, unsteady and random and it comprises a wide range of scales which exchange energy between them. For fully turbulent flows at high Reynolds number, the energetic interaction between the different turbulent scales can be described by the theory of the energy cascade proposed by [Richardson, 1922](#), which was later completed by the Kolmogorov's hypotheses ([Kolmogorov, 1941](#)). Large-Eddy Simulation is based on the idea that the energy containing largest scales or eddies, which are anisotropic and strongly dependent on the boundary conditions of the flow, are explicitly resolved, while the smallest eddies, which have an isotropic and a more universal character, can be modeled. A mathematical representation of this scale separation operation can be provided by the convolution filtering approach proposed by [Leonard, 1975](#). Thus, the governing equations are filtered and later resolved for the filtered flow field quantities. Different terms arise from the filtering process (in analogy to the Reynolds stresses in the RANS approach) known as Sub-Grid Scale (SGS) terms, which represent the effect of the smallest scales on the motion of the largest eddies. In order to close the problem such terms need modeling. Different models for the SGS stress tensor have been proposed, from the explicit functional and structural approaches, to the implicit modeling or Implicit LES (ILES). Some of the SGS models used for compressible flows are presented in [Garnier et al., 2009](#). Each section of the current chapter describes one of the aforementioned arguments.

### 2.1 Energy cascade and Kolmogorov hypotheses

According to the theory of [Richardson, 1922](#), the motion of the largest eddies in a fully turbulent flow at high Reynolds number is unstable and this results in these eddies splitting into smaller ones. During the splitting, energy is transferred from the former to the latter and this process repeats itself down to smaller and smaller scales, until the Reynolds number is sufficiently low that the molecular viscosity irreversibly dissipates the available kinetic energy into internal energy and the motion of the eddies becomes stable. Thus, a certain mechanism is attributed to each scale of turbulent motion: energy production to the largest eddies, energy transfer to the intermediate eddies and energy dissipation to the smallest ones.

Kolmogorov, 1941 completed the theory introducing three fundamental hypothesis:

- **Hypothesis zero of local isotropy:** At sufficiently high Reynolds number, the small scales of turbulent motion are statistically isotropic.
- **First similarity hypothesis:** At sufficiently high Reynolds number, the statistics of the small scales of turbulent motion have a universal form that is uniquely determined by the energy dissipation  $\epsilon$  and the kinematic viscosity  $\nu$ .
- **Second similarity hypothesis:** At sufficiently high Reynolds number, the statistics of the intermediate scales of turbulent motion have a universal form that is uniquely determined by  $\epsilon$  and is independent of  $\nu$ .

According to Kolmogorov, the largest eddies are strongly anisotropic and dependent on the boundary conditions of the flow. Also, the bulk of the energy is contained in these eddies. But, during the cascade-like formation process of the smaller eddies, the directional and geometry information of the large ones fades away. This results in the small scales of the turbulent motion having an isotropic and a more universal nature. Since the mechanisms attributed to these scales are the energy transfer and viscous dissipation, the parameters that characterize them are the rate at which smaller eddies receive energy from the larger ones  $T_E$  and the kinematic viscosity  $\nu$ . It can be demonstrated that  $T_E \approx \epsilon$  with  $\epsilon$  being the energy dissipation, that is the rate at which energy is transferred from the large eddies to the smaller ones equals the rate at which the energy is dissipated by the smallest eddies. Moreover, the timescales of the smaller eddies are relatively too small compared to the timescales of the large ones, therefore the former can adapt quickly to the transfer of energy received from the latter. As a result of the previous affirmations, the turbulent motion scales range is split into an energy containing range for the large scales and a universal equilibrium range for the small ones.

The two parameters  $\epsilon$  and  $\nu$  can be used to define three unique scales for length, velocity and time defined as:

$$\eta = \left(\frac{\nu^3}{\epsilon}\right)^{1/4} \quad (2.1)$$

$$u_\eta = (\epsilon\nu)^{1/4} \quad (2.2)$$

$$\tau_\eta = \left(\frac{\nu}{\epsilon}\right)^{1/2} \quad (2.3)$$

The fact that the Reynolds number for these scales is unity:  $Re = \frac{u_\eta \eta}{\nu} = 1$ , and that combining (2.1) and (2.2) gives:  $\epsilon = \nu \left(\frac{u_\eta}{\eta}\right)^2$ , demonstrates that these scales represent the smallest eddies at the bottom of the cascade, since there the kinetic energy is irreversibly dissipated into internal energy due to the fact that molecular viscosity becomes preponderant and the splitting into smaller eddies stops. These scales are known in literature as the Kolmogorov's scales.

Considering that  $T_E \approx \epsilon$ , this results in  $\epsilon \sim \frac{u_0^3}{l_0}$ , where  $l_0$ ,  $u_0$  and  $\tau_0$  are respectively the characteristic length, velocity and time of the largest eddies, which are comparable to the characteristic scales of the flow:  $\mathcal{L}, \mathcal{U}, \mathcal{T}$ . Therefore, the Reynolds number of the largest eddies is of the same order as the Reynolds number of the flow:  $Re_0 \sim Re$ . From these last assertions and the definitions (2.1)-(2.3), one can easily determine the ratios between the Kolmogorov's scales and the largest scales as:

$$\frac{\eta}{l_0} \sim Re^{-3/4} \quad (2.4)$$

$$\frac{u_\eta}{u_0} \sim Re^{-1/4} \quad (2.5)$$

$$\frac{\tau_\eta}{\tau_0} \sim Re^{-1/2} \quad (2.6)$$

Thus, it is evident as all scales characterizing the smallest eddies decrease with increasing Reynolds number of the flow.

Moreover, within the universal equilibrium range, eddies of size  $l$  exist such that  $\eta \ll l \ll l_0$ , for which the Reynolds number is still too high compared to the Kolmogorov's scales. So, little does molecular viscosity effect these eddies, whose character is thus defined only by the energy dissipation  $\epsilon$ . This further separation within the small eddies splits the universal equilibrium range into an inertial subrange where the molecular viscosity is negligible with reference to inertial effects, and a dissipation range where the molecular viscosity becomes effective. A direct consequence of the Kolmogorov's hypotheses is that the characteristic velocity and timescale decrease with eddies size in the inertial subrange. It can also be demonstrated that the energy transfer rate  $T(l)$  in this subrange is independent of  $l$ :  $T(l) = T = T_E = \epsilon$ . A schematic representation of the energy cascade in a fully turbulent flow at high Reynolds number is given in Fig. 2.1.

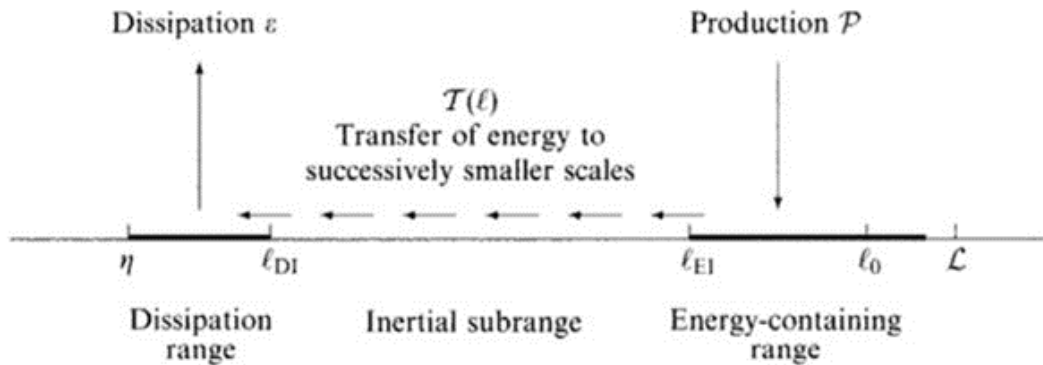


**Figure 2.1:** Schematic representation of the energy cascade in a fully turbulent flow at high Reynolds number (Pope, 2001).

Finally, in order to determine how the kinetic energy is distributed among the different scales of turbulent motion, the energy spectrum in the wavenumber space can be defined in the case of homogeneous turbulence (Fig. 2.2). In the spectral

space the wavenumber is defined as:  $k = \frac{2\pi}{l}$ . Kolmogorov proposed the following law, based on the second hypothesis of similarity, to describe the energy cascade in the inertial subrange:  $E(k) = C\epsilon^{2/3}k^{-5/3}$ , with  $C$  being a universal constant. In the energy containing range the slope of the spectrum varies between  $k$  and  $k^4$  (Garnier et al., 2009).

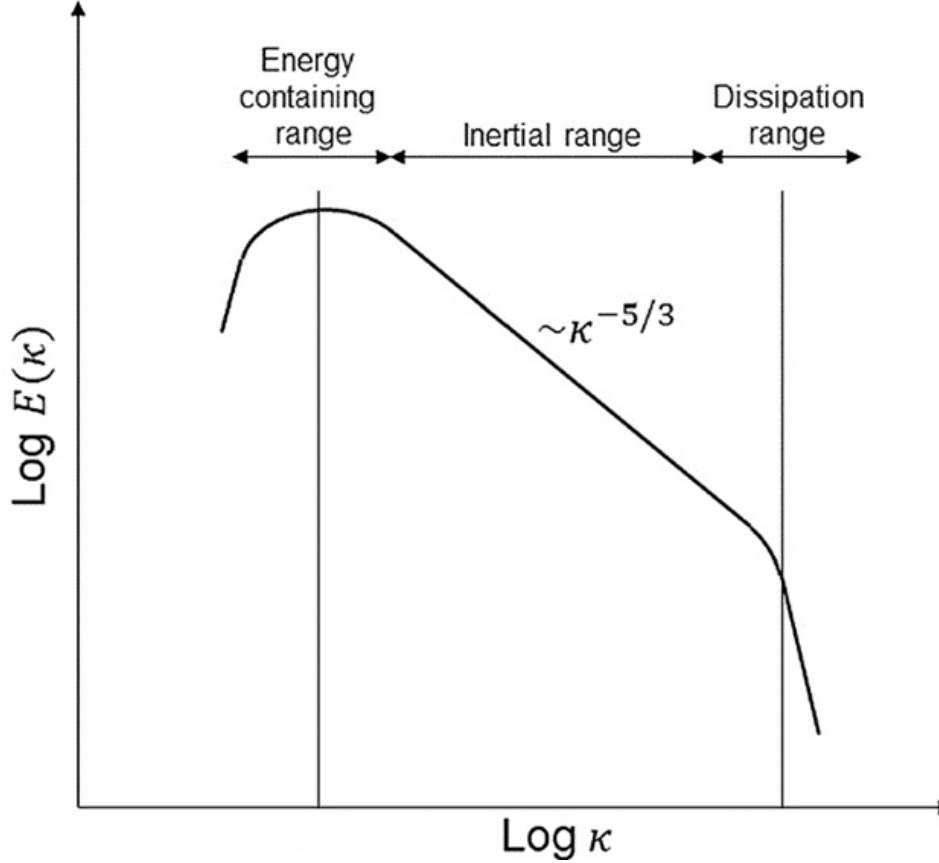


**Figure 2.2:** Energy spectrum for homogeneous turbulence (Kalmár-Nagy and Bak, 2019).

However, as far as turbomachinery flows are concerned, the turbulent motion inside an aeronautical engine is strongly anisotropic and inhomogeneous, therefore this kind of simplified theory fails to accurately predict the interaction and energy distribution between different turbulent scales. Moreover, energy can also be transferred from the smaller eddies to the larger ones. This kind of inverse energy transfer is defined as backscatter and generally is much smaller in intensity if compared to the outscatter. Nevertheless, simplified theories as Kolmogorov's are used to make important considerations which can be useful for a better understanding of some of the aspects of turbulence nature, while recurring to numerical methods in order to obtain an accurate and realistic representation of turbulent flows.

## 2.2 The Large-Eddy Simulation approach

In order to obtain the full solution for the whole range of scales of turbulent motion, a Direct Numerical Simulation must be performed. According to the DNS approach, the governing equations must be solved directly without introducing any turbulence model. Therefore, the computational grid must be fine enough in order to capture even the smallest Kolmogorov scales. For typical engineering flows though, this would require a grid resolution that exceeds the current computing capacities.

In an attempt to reduce the simulation's computational cost, a coarser grid can be considered. This way, only scales larger than the grid size would be represented, whereas the smaller scales would be discarded. If the governing equations were still to be solved directly, without any turbulence model, the solution obtained would generally be inaccurate from a physical point of view due to the continuous non-linear energetic interaction between all scales of turbulent motion. Thus, in order to maintain the reduced grid resolution, the effect of the smallest unrepresented scales on the motion of the largest represented eddies must be modeled and this constitutes the basic idea of the Large-Eddy Simulation approach.

Such scale separation in the range of scales of turbulent motion is consistent with the Kolmogorov's theory described in the previous chapter. According to such theory, the largest eddies of the turbulent motion contain most of the kinetic energy and are strongly anisotropic and fluid dependent, whereas the smaller scales are of isotropic and universal nature. So, the LES approach relies on the idea that an approximate solution can be obtained by resolving the motion of only the largest eddies in the range of turbulent scales, where the vast part of the energy is concentrated, while modeling the effects of the smallest ones. Since the latter present a more universal character, their modeling is expected to be easier and have a relatively minor impact on the solution accuracy, as compared to RANS turbulence closure modeling, where all scales of turbulent motion are modeled within the method (Fig. 2.3). Moreover, the LES solution conserves the three-dimensional, unsteady nature of turbulent motion, making this method viable to study flows where the large-scale unsteadiness is important and the RANS approach would fail to predict an accurate solution.

Finally, after a turbulence model is introduced, the governing equations for LES simulations are then discretized by means of some numerical method. Such numerical method presents a scale dependent truncation error in time and space, which especially affects the smallest represented scales. Therefore, the discretization method used introduces a further separation between well-resolved represented scales and non-resolved represented scales, where the latter are also known in literature as resolved sub-filter scales.

The main problem in LES is to define a mathematical model that describes and accounts for all the physical aspects of the turbulent flow motion and to model all the previously mentioned scale subranges. The mathematical model and the discretization method are strongly connected to each other and usually their definition is carried out simultaneously. Therefore, the definition of a relaxation

between the strong link that lies between these two very important aspects of the LES approach is not trivial.

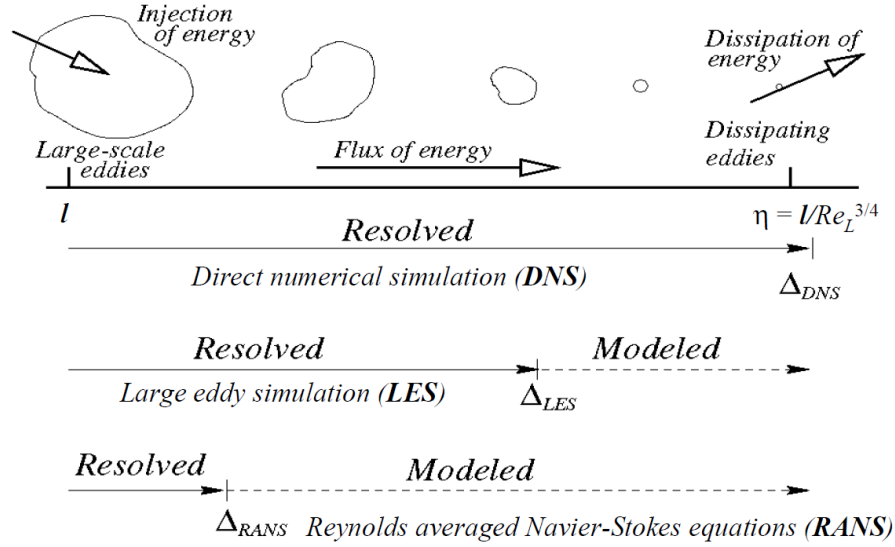


**Figure 2.3:** Comparison between different simulation approaches for turbulent flows according to the scales of eddies resolved within the model (Pope, 2001).

### 2.2.1 Governing equations

As for any turbulence problem, the Navier-Stokes equations are usually used in the LES approach to define its mathematical model. These equations represent the conservation of mass, momentum and energy, with the last one not being unique. Indeed, many formulations of this equation have been proposed in the field of LES for compressible flows in terms of temperature, pressure, enthalpy, entropy or total energy, with the last one being the only one in the conservative form (Garnier et al., 2009). Considering the formulation in terms of total energy, the Navier-Stokes equations take the following form:

$$\frac{\partial \rho}{\partial t} + \frac{\partial \rho u_j}{\partial x_j} = 0 \quad (2.7)$$

$$\frac{\partial \rho u_i}{\partial t} + \frac{\partial \rho u_i u_j}{\partial x_j} + \frac{\partial p}{\partial x_i} = \frac{\partial \sigma_{ij}}{\partial x_j} \quad (2.8)$$

$$\frac{\partial \rho E}{\partial t} + \frac{\partial (\rho E + p) u_j}{\partial x_j} = \frac{\partial \sigma_{ij} u_i}{\partial x_j} - \frac{\partial q_j}{\partial x_j} \quad (2.9)$$

The set of equations is complemented with the perfect gas equation of state:

$$p = \rho RT \quad (2.10)$$

The Einstein notation has been adopted.  $t$  and  $x_i$  represent the independent variables of time and space respectively with  $i = \{1, 2, 3\}$  denoting the three directions of the Cartesian coordinate system.  $u_i$ ,  $p$ ,  $\rho$ ,  $T$  are the velocity components,

pressure, density and temperature. The gas constant is defined as:  $R = C_p - C_v$ , where  $C_p$  and  $C_v$  are respectively the specific heats at constant pressure and constant volume, connected together by the relation:  $\gamma = \frac{C_p}{C_v}$ , with  $\gamma$  being the isentropic expansion factor.

Considering a Newtonian fluid and assuming the Stokes' hypothesis for the bulk viscosity, the shear-stress tensor can be expressed as:

$$\sigma_{ij} = 2\mu(T)S_{ij} - \frac{2}{3}\mu(T)\delta_{ij}S_{kk} \quad (2.11)$$

where  $\mu(T)$  is the dynamic viscosity,  $\delta_{ij}$  is the function delta Dirac and  $S_{ij}$  represents the rate-of-strain tensor defined as:

$$S_{ij} = \frac{1}{2} \left( \frac{\partial u_i}{\partial x_j} + \frac{\partial u_j}{\partial x_i} \right) \quad (2.12)$$

The total energy per mass unit is defined as:

$$\rho E = \frac{p}{\gamma - 1} + \frac{1}{2}\rho u_i u_i \quad (2.13)$$

Finally, the heat flux can be expressed according to the Fourier's law as:

$$q_j = -\lambda(T) \frac{\partial T}{\partial x_j} \quad (2.14)$$

where  $\lambda = \frac{\mu C_p}{Pr}$  is the thermal conductivity and  $Pr$  is the Prandtl number.

In order to obtain an approximate solution, this set of equations must be solved for the motion of only the large eddies of the turbulent motion, while modeling the effects of the smallest ones. In practical LES simulations, this scale separation operation is implicitly carried out by the finite-size computational grid itself, since scales smaller than the grid size cannot be represented. Once a turbulence closure model that accounts for the presence of the smallest unrepresented scales is introduced, the governing equations are then discretized by means of a certain numerical method. Both turbulence and numerical methods are characterized by intrinsic physical and numerical errors respectively. These errors have a strong impact especially on the smallest represented scales. Thus, a further separation between well-resolved scales and sub-filter scales is presented. The final solution can then be interpreted as an approximation obtained by applying an overall filtering operation to the real exact solution of the governing equations system, focalizing the full picture only on the largest eddies, while lowering its resolution by eliminating the presence of the smallest ones.

Such filtering operation could be represented mathematically by the convolution filtering approach proposed by [Leonard, 1975](#). However, the actual filter applied to the exact solution comprises all the different kinds of filters implicitly carried out by the grid and numerical method and eventual filters explicitly introduced by the turbulence model, as will be described in the following sections. Therefore, it is no trivial task finding the shape of the effective filter applied by the LES approach. Actually, it is important to point out that the filtering approach is

a purely mathematical analysis tool which helps to comprehend the physics of the problem, while trying to imitate what is actually done in real practical LES. Generally though, no explicit filtering operation is actually applied to the flow field variables that appear in the governing equations, except for trivial cases where the turbulence models require so.

### 2.2.2 Convolution filtering operation

The convolution filtering approach proposed by [Leonard, 1975](#) consists in applying a high-pass filter in physical space (or a low-pass filter in wavenumber space) to the Navier-Stokes equations (2.7)-(2.9) and to all of the flow field quantities that appear in these equations.

Limiting the case study to homogeneous and isotropic filtering for sake of simplicity, the three-dimensional convolution filtering in space applied to a scalar quantity  $\phi(\mathbf{x}, t)$  is defined as followed:

$$\bar{\phi}(\mathbf{x}, t) = \int_{-\infty}^{\infty} G(\mathbf{x} - \boldsymbol{\xi}) \phi(\boldsymbol{\xi}, t) d^3 \boldsymbol{\xi} \quad (2.15)$$

where  $G$  is a compactly supported or at least rapidly decaying filter function in space, with a filter width  $\Delta$ . Symbolically, the previous equation can be expressed as:

$$\bar{\phi} = G * \phi \quad (2.16)$$

The relation (2.15) can also be expressed in the wavenumber space where the cutoff wavenumber associated to the filter width is defined as  $k_c = \frac{\pi}{\Delta}$ . This can be helpful since the Fourier transform of a convolution between two functions  $\phi(\mathbf{x}, t)$  and  $G(\mathbf{x})$  in physical space is nothing else but the product of the Fourier transforms of the two functions, denoted as  $\hat{\phi}(\mathbf{k}, \omega)$  and  $\hat{G}(\mathbf{k})$ , where  $\mathbf{k}$  and  $\omega$  are the wavenumber and frequency respectively:

$$\hat{\bar{\phi}}(\mathbf{k}, \omega) = \hat{G}(\mathbf{k}) \hat{\phi}(\mathbf{k}, \omega) \quad (2.17)$$

or:

$$\bar{\hat{\phi}} = \hat{G} \hat{\phi} \quad (2.18)$$

Furthemore, the unfiltered part of the scalar quantity  $\phi(\mathbf{x}, t)$  can be defined as:

$$\phi'(\mathbf{x}, t) = \phi(\mathbf{x}, t) - \bar{\phi}(\mathbf{x}, t) \quad (2.19)$$

$$\phi' = (1 - G) * \phi \quad (2.20)$$

Not every kind of filter can be considered while defining a mathematical model of the LES approach, for specific requirements must be met in order to adequately manipulate the Navier-Stokes equations. The fundamental properties that a LES filter function must satisfy are:

- **Consistency:**

$$\int_{-\infty}^{\infty} G(\boldsymbol{\xi}) d^3 \boldsymbol{\xi} = 1 \quad (2.21)$$

- **Linearity:**

$$\overline{\phi + \psi} = \bar{\phi} + \bar{\psi} \quad (2.22)$$

- **Commutation with differentiation:**

$$\frac{\partial \bar{\phi}}{\partial s} = \bar{\frac{\partial \phi}{\partial s}}, \quad s = \mathbf{x}, t \quad (2.23)$$

It is also important to highlight the differences between the convolution filtering operator and the Reynolds averaging operator. The latter satisfies the following properties:

$$\langle a\phi \rangle = a\langle \phi \rangle \quad (2.24)$$

$$\langle \phi + \psi \rangle = \langle \phi \rangle + \langle \psi \rangle \quad (2.25)$$

$$\left\langle \frac{\partial \phi}{\partial s} \right\rangle = \frac{\partial \langle \phi \rangle}{\partial s}, \quad s = \mathbf{x}, t \quad (2.26)$$

$$\langle \langle \phi \rangle \rangle = \langle \phi \rangle \quad (2.27)$$

$$\langle \phi' \rangle = 0 \quad (2.28)$$

What clearly distinguishes the filtering in LES from the Reynolds averaging operator is that the convolution filtering operator does not satisfy the properties expressed in (2.27)-(2.28), except in trivial cases, that is:

$$\bar{\bar{\phi}} = G * G * \phi \neq \bar{\phi} \quad (2.29)$$

$$\bar{\phi}' = G * (1 - G) * \phi \neq 0 \quad (2.30)$$

The most diffused filters used to make considerations in the LES approach are: the Gaussian filter, the sharp cutoff filter and the box or top-hat filter. A representation of their filter functions in both physical and wavenumber space is provided in Fig. 2.4 for the same filter width (cutoff wavenumber).

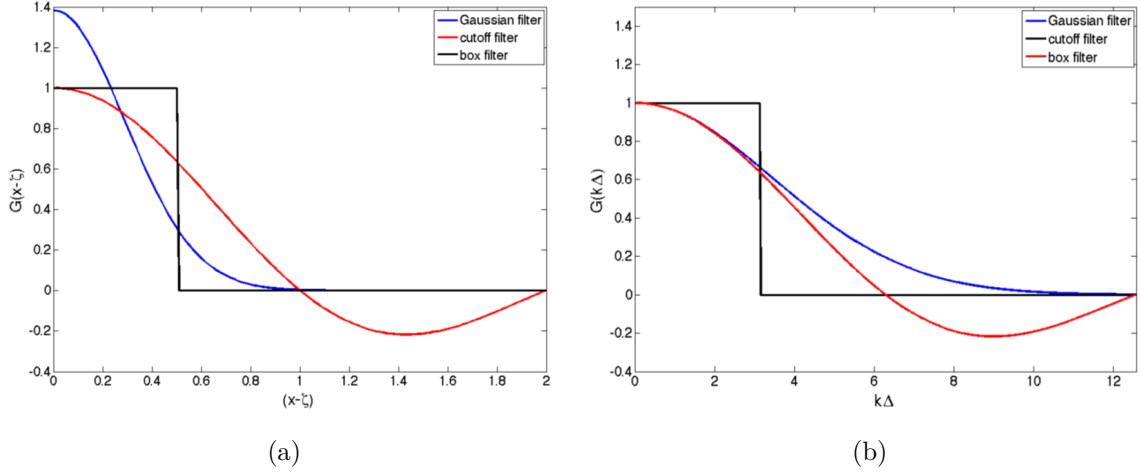


**Figure 2.4:** Gaussian, cutoff and box filters plotted for the same filter width (cutoff wavenumber): (a) in physical space and (b) in wavenumber space (Stoll, 2014).

In order to interpret the filtering operation in physical space, a one-dimensional case and the velocity component  $u(x, t)$  are considered. Spatially filtering the instantaneous velocity  $u(x, t)$ , say with a box filter, will smoothen the velocity function just as shown in Fig. 2.5, by removing the presence of the smallest scales from the solution. According to (2.15), the function  $\bar{u}$  is a continuous function and it represents an approximation to what is actually obtained when a discretization method is applied to solve the governing equations system on a discrete grid.

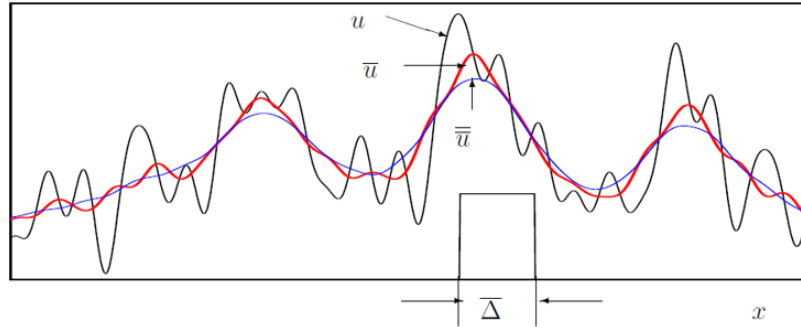


**Figure 2.5:** Box filter applied to the velocity component in physical space in a one-dimensional case (Fröhlich and Rodi, 2002).

In the same figure, the double filtered velocity is also represented, thus making it clear how the filtering process would keep smoothening the velocity function if reapplied, in contrary to the RANS averaging operation where the double averaged quantity equals the averaged quantity itself. The cutoff filter is a trivial case in which the property (2.27) is satisfied, that is in this case:  $\bar{\bar{u}} = \bar{u}$ .

On the other hand, the concept of filtering in wavenumber space can be interpreted by considering the energy spectrum in the case of homogeneous and isotropic

turbulence. Referring to a DNS-resolved field (no filter case), different filters at the same cutoff wavenumber are applied to the flow field solution and the filtered shapes of the energy spectrum are represented in Fig. 2.6.

The cutoff filter is the only filter that yields a neat cut through the energy spectrum. This way the filtered energy spectrum presents, at the cutoff, the same slope as the unfiltered one, with the same energy transfer rate as the dissipation of the smallest scales. Contrarily, other filters present different slopes with different rates of energy transfer and it is clear how the top hat filter for instance fails in attenuating the energy of the sub-grid scales.

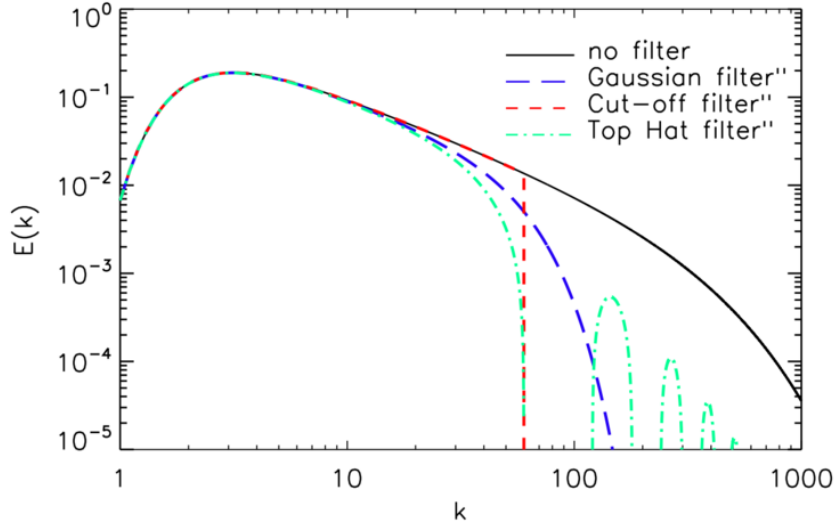


**Figure 2.6:** Comparison between different filters applied to the energy spectrum in case of homogeneous and isotropic turbulence (Laval, 2020).

### 2.2.3 Favre filtering

Before proceeding with the definition of the filtered Navier-Stokes equations, another important "filtering" process needs to be introduced. That is the Favre filtering, according to which a change of variable is defined where the filtered variables are weighted by the density:

$$\tilde{\phi} = \frac{\overline{\rho\phi}}{\bar{\rho}} \quad (2.31)$$

An evident analogy exists between Favre filtering and Favre averaging used in the field of compressible RANS.

The introduction of the Favre filtered variables in the Navier-Stokes equations is important due to terms of the form  $\rho\phi$  and  $\rho\phi\psi$  being present in the system of equations. Introducing the Favre change of variables, such terms can be expressed as:

$$\overline{\rho\phi} = \bar{\rho}\tilde{\phi} \quad (2.32)$$

$$\overline{\rho\phi\psi} = \bar{\rho}\widetilde{\phi\psi} \quad (2.33)$$

This way, one can avoid the introduction of some residual terms in the filtered Navier-Stokes equations, which would appear due to the non-commutative nature of the convolution filtering operator with the multiplication operator.

### 2.2.4 Filtered governing equations

Applying the convolution filtering operator to the Navier-Stokes equations (2.7)-(2.9), by simultaneously introducing the Favre change of variables and resolving the non-linear equations system only for computable flow field quantities, the following system of equations is obtained:

$$\frac{\partial \bar{\rho}}{\partial t} + \frac{\partial \bar{\rho} \tilde{u}_j}{\partial x_j} = 0 \quad (2.34)$$

$$\frac{\partial \bar{\rho} \tilde{u}_i}{\partial t} + \frac{\partial \bar{\rho} \tilde{u}_i \tilde{u}_j}{\partial x_j} + \frac{\partial \bar{p}}{\partial x_i} - \frac{\partial \check{\sigma}_{ij}}{\partial x_j} = -\frac{\partial \tau_{ij}}{\partial x_j} + \frac{\partial (\bar{\sigma}_{ij} - \check{\sigma}_{ij})}{\partial x_j} \quad (2.35)$$

$$\frac{\partial \bar{\rho} \tilde{E}}{\partial t} + \frac{\partial (\bar{\rho} \tilde{E} + \bar{p}) \tilde{u}_j}{\partial x_j} - \frac{\partial \check{\sigma}_{ij} \tilde{u}_i}{\partial x_j} + \frac{\partial \check{q}_j}{\partial x_j} = -\frac{\partial}{\partial x_j} [C_p \mathcal{Q}_j + \mathcal{J}_j - \mathcal{D}_j + (\bar{q}_j - \check{q}_j)] \quad (2.36)$$

The terms on the left hand side represent the computable terms of the equations system and they are structurally identical to the original unfiltered governing equations, except for the fact that they contain filtered variables. Diversely, the right hand side regroups the residual terms that appear due to the non-linearities present in the Navier-Stokes equations, such as the convective term. The residual terms are widely known in literature as Sub-Grid Scale terms and physically they represent the effect that the smallest turbulent scales have on the motion of the largest eddies.

The filtered equation of state becomes:

$$\bar{p} = \bar{\rho} R \tilde{T} \quad (2.37)$$

The Favre filtering can be applied to the temperature, but not to the pressure and density fields.  $\tilde{u}_i$ ,  $\bar{p}$ ,  $\bar{\rho}$ ,  $\tilde{T}$  represent the computable velocity components, pressure, density and temperature respectively.

The computable shear-stress tensor is defined as:

$$\check{\sigma}_{ij} = 2\mu(\tilde{T})\tilde{S}_{ij} - \frac{2}{3}\mu(\tilde{T})\delta_{ij}\tilde{S}_{kk} \quad (2.38)$$

where  $\tilde{S}_{ij}$  is the computable rate-of-strain tensor:

$$\tilde{S}_{ij} = \frac{1}{2} \left( \frac{\partial \tilde{u}_i}{\partial x_j} + \frac{\partial \tilde{u}_j}{\partial x_i} \right) \quad (2.39)$$

The computable total energy per mass unit is defined according to the following formulation:

$$\bar{\rho}\tilde{E} = \frac{\bar{p}}{\gamma - 1} + \frac{1}{2}\bar{\rho}\tilde{u}_i\tilde{u}_i + \frac{\tau_{ii}}{2} \quad (2.40)$$

The computable heat flux is expressed as:

$$\check{q}_j = -k(\tilde{T})\frac{\partial\tilde{T}}{\partial x_j} \quad (2.41)$$

Considering now the SGS terms, these are:

- **SGS stress tensor:**

$$\tau_{ij} = \bar{\rho}\widetilde{u_i u_j} - \bar{\rho}\tilde{u}_i\tilde{u}_j \quad (2.42)$$

- **SGS shear-stress tensor error:**

$$\bar{\sigma}_{ij} - \check{\sigma}_{ij} = \overline{2\mu(T)S_{ij} - \frac{2}{3}\mu(T)\delta_{ij}S_{kk} - \check{\sigma}_{ij}} \quad (2.43)$$

- **SGS temperature flux:**

$$\mathcal{Q}_j = \bar{\rho}\widetilde{u_j T} - \bar{\rho}\tilde{u}_j\tilde{T} \quad (2.44)$$

- **SGS turbulent diffusion:**

$$\mathcal{J}_j = \frac{1}{2}(\overline{\rho\widetilde{u_j u_i u_i}} - \bar{\rho}\tilde{u}_j\tilde{u}_i\tilde{u}_i - \tilde{u}_j\tau_{ii}) \quad (2.45)$$

- **SGS viscous diffusion:**

$$\mathcal{D}_j = \overline{\sigma_{ij}u_i} - \check{\sigma}_{ij}\tilde{u}_i \quad (2.46)$$

- **SGS heat flux error:**

$$\bar{q}_j - \check{q}_j = \overline{-k(T)\frac{\partial T}{\partial x_j}} - \check{q}_j \quad (2.47)$$

The filtered governing equations system described in the current section has been defined by expressing the filtered total energy as in equation (2.40). It is important to mention that this formulation is not unique, for other formulations have been proposed in literature which consist in a change of variables on the filtered pressure or temperature, or both (Garnier et al., 2009). Subsequently, the Navier-Stokes equations are filtered according to the definitions adopted for the filtered thermodynamic variables and different SGS terms appear in each of the formulations. Furthermore, as mentioned in section 2.2.1, the energy equation can also be expressed in terms of temperature, pressure, enthalpy or entropy. Different studies in literature show that, depending on the formulation adopted, the different SGS terms that appear have different amplitudes. However, these studies were

performed only for certain cases of flow simulations, therefore no universal reliability of the results is guaranteed.

With reference to the incompressible LES problem where the SGS stress tensor is the only residual term present, in the current definition of the filtered governing equations five more SGS terms appear. These terms represent the effect of the smallest unresolved scales on the motion of the largest resolved eddies. Therefore, in order to close the problem and obtain a physically accurate solution while resolving the governing equations, these terms need to be modeled. Turbulence closure models for LES are widely known in literature as SGS models.

### 2.2.5 SGS modeling

The SGS modeling consists in approximating the residual terms that appear in the filtered governing equations system. These terms represent the error committed by considering filtered computable variables in the system of equations, rather than the filtered fields of non-linear terms present in the original Navier-Stokes equations. From a physical point of view these terms arise on account of smallest scales of turbulent motion not being represented by the computational grid. Their presence cannot be neglected though, due to the continuous non-linear energetic interaction between all scales of turbulent motion. The SGS modeling idea relies on approximating these scales, or at least their effect on the motion of the largest resolved eddies, on the basis of information contained or assumptions made on the latter.

A vast part of the available SGS models are defined in the framework of homogeneous and isotropic turbulence, thus making use of Kolmogorov's theory that describes the non-linear energy distribution between the different turbulent scales of the energy cascade. The separation between represented and unrepresented scales on the computational grid can be interpreted as a cutoff filter applied to the energy spectrum in the wavenumber space. The cutoff wavenumber associated to the grid size is usually supposed to be located within the inertial subrange of the energy cascade.

Moreover, the smallest represented scales near the cutoff are afflicted by an energy attenuation due to the truncation errors introduced by the numerical scheme used to discretize the differential operators. Therefore, a further separation between well-resolved and unresolved scales is introduced within the presented scales subrange, where the latter are also referred to as resolved subfilter scales (Fig. 2.7). According to Pope, 2001, a well-resolved LES must be able to solve at least 80% of the kinetic energy of the turbulent motion. Another indicator on LES reliability is the absence of any eventual energy accumulation at scales near the cutoff.

The different SGS models proposed up to date are classified under two main categories: functional and structural modeling approaches. The functional approach consists in modeling the impact that the unresolved eddies have on the resolved ones, without attempting to reconstruct the former. This way, a part of the information contained in the structure of the smallest eddies is lost. On the other hand, according to the structural approach, an approximation of the unfiltered field

can be obtained from considerations made based on the filtered solution. Therefore, no knowledge on the nature of interaction between scales is required.

Up to date, various models of the SGS stress tensor have been proposed. Most of them are defined in the incompressible case and have usually been extended to compressible problems by adopting the incompressibility hypothesis of the smallest universal scales of turbulent motion (Garnier et al., 2009).

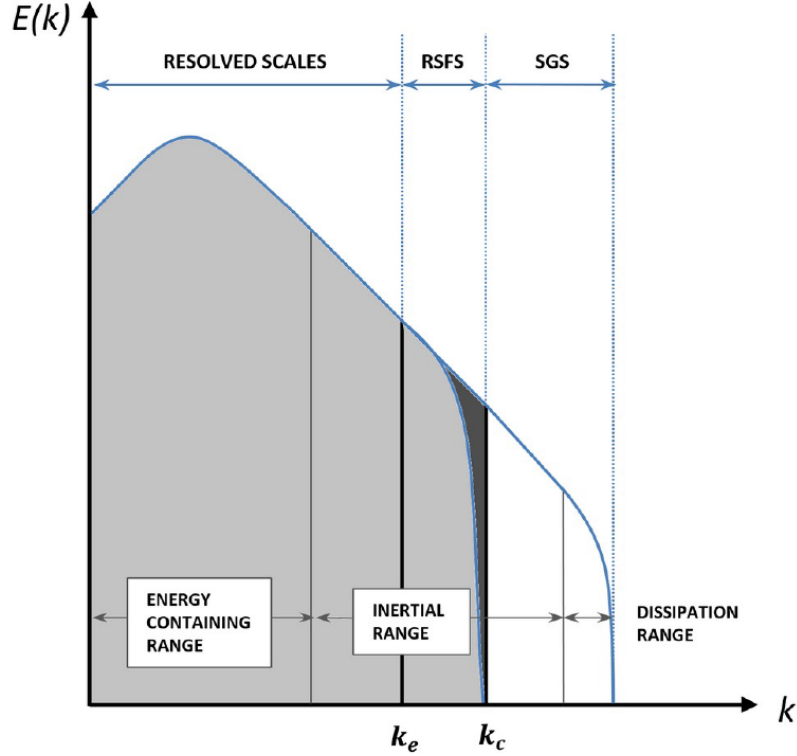


**Figure 2.7:** Representation of different scale subranges in LES for homogeneous and isotropic turbulence (Maulik and San, 2018).

### Functional modeling

The functional modeling is based on the idea that the interaction between sub-grid and resolved scales is of energetic nature. Therefore, the sole balance of the energy transfer between the two scale subranges is sufficient to describe the impact that the former have on the latter. In practice, this kind of modeling consists in introducing additional terms in the governing equations, which reproduce the desired dissipation (or energy production in the case of backscatter) that emulates the aforementioned energetic interaction. This can either be done explicitly by introducing additional terms to the equations, or implicitly by adjusting the discretization scheme in such a way that the numerical error introduced produces the desired dissipation. Simulations based on the second approach are referred to as Implicit LES (ILES).

A very popular framework of explicit functional models for the SGS stress tensor consists of the eddy-viscosity models. This approach makes use of the **Boussinesq**

**hypothesis** which affirms that: *The energy transfer mechanism from resolved to subgrid scales is analogous to molecular mechanisms represented by the diffusion term, in which the molecular viscosity appears.* According to this assumption (Boussinesq, 1877), the deviatoric part of the SGS stress tensor can be expressed in a similar way to the molecular diffusion term:

$$\tau_{ij}^d = \tau_{ij} - \frac{1}{3}\delta_{ij}\tau_{kk} = -2\bar{\rho}\nu_{sgs} \left( \tilde{S}_{ij} - \frac{1}{3}\delta_{ij}\tilde{S}_{kk} \right) \quad (2.48)$$

where  $\tau_{kk}$  is the isotropic part of the SGS stress tensor and  $\nu_{sgs}$  is the eddy-viscosity introduced by the Boussinesq hypothesis.

One of the most famous and most diffused eddy-viscosity models is the one proposed by Smagorinsky, 1963, according to whom the eddy-viscosity can be computed from characteristic lengthscales and the resolved rate-of-strain tensor magnitude as:

$$\nu_{sgs} = C_s^2 \Delta^2 |\tilde{S}| \quad (2.49)$$

where  $|\tilde{S}|$  is the rate-of-strain tensor characteristic:

$$|\tilde{S}| = (2\tilde{S}_{ij}\tilde{S}_{ij})^{1/2} \quad (2.50)$$

while  $C_s$  is the Smagorinsky constant and  $\Delta$  represents the grid size.

Different studies have demonstrated that the Smagorinsky constant is not single-valued, but depends on the type of the flow. Other than being fluid dependent, the Smagorinsky model is overly dissipative and is inapplicable in near-wall regions and transitional flows. In spite of the aforementioned drawbacks, it still is one of the simplest SGS stress tensor models and its ease of implementation makes it preferable over other approaches.

In order to improve the Smagorinsky model, Germano et al., 1991 proposed a dynamic approach that allows a self adaptive estimation of the Smagorinsky constant from the simulation itself, by explicitly applying a test filter with  $\Delta_t > \Delta$  to the SGS stress tensor. His model was further improved by Lilly, 1992, who proposed to calculate  $C_s$  by a least-mean square method. This procedure is very general with reference to the simple Smagorinsky model and the time and space dependent nature of the  $C_s$  coefficient, defined according to the dynamic formulation, allows for a higher accuracy to be achieved.

## Structural modeling

While the functional approach consists in modeling the effects of the unresolved scales on the resolved ones, the structural approach on the other hand relies on the idea that the unfiltered field can be reconstructed from the filtered one. One of the most diffused structural models is the so called Approximate Deconvolution Method (ADM). According to this approach, an approximation of the unfiltered field is obtained by means of truncated series expansion of the inverse filter operator applied to the filtered flow field quantities. In this case, a well defined filter is considered.

Furthermore, in order to improve the stability of the method, a regularization technique can be used along with the ADM. Different regularization techniques include explicit filtering or eddy-viscosity regularization. According to the former approach a secondary filter, with a filter width greater than the grid size, is applied at the end of each iteration in order to eliminate wavenumbers higher than the cutoff wavenumber in the approximated solution provided by the ADM. This way, the problem of accumulated kinetic energy at the cutoff is overcome. However, the explicit filtering approach reduces the effective resolution of the simulation compared to the dynamic range supported by the mesh, since the filter width is greater than the grid size (Lund, 2003), and this results in a considerable increase in computational cost.

### Implicit modeling

As all practical simulations, LES approach consists in resolving the governing equations system on a discrete grid by means of some numerical method. The finite spatial resolution of the grid implicitly induces a scale separation within the range of scales of turbulent motion, since eddies smaller than the grid size cannot be represented. Moreover, the numerical scheme used to discretize the differential operators introduces a scale dependent truncation error in time and space. The main idea of ILES models is that the truncation error of the numerical scheme could be modeled in such a way that it would provide the necessary amount of dissipation that emulates the energetic interaction between represented and unrepresented scales on the computational grid. Therefore, there is no need to explicitly introduce a SGS model, since the numerical scheme discretization error itself behaves as a SGS term.

Many different approaches have been proposed in the field of ILES modeling, from the very first Volume Balance Procedure, to much more sophisticated theories such as Adaptive Local Deconvolution Method. Even though their application in the field of LES has given reliable results and promising performances, an important drawback consists in the lack of possibility of a direct control on the numerical error and the strong coupling that now exists between the physical model and the discretization scheme.

## 2.3 Concluding remarks

It is important to highlight that the convolution filtering approach was introduced in order to analytically address some of the aspects of the LES theory, such as the SGS closure modeling. However, in most practical LES simulations no explicit filtering is performed on the flow field variables, except for in trivial cases where the filtering process is required in any of the SGS models adopted, such as in the explicit filtering regularization method or the Germano's dynamic model test filter. In any case, whether the filtering process is explicit or not, the terminology "explicit modeling" refers to all those methods where the SGS effects are modeled by explicitly introducing additional terms in the governing equations.

In this kind of approach, the choice of a turbulence model and a discretization scheme must be handled with care, since errors introduced by both models interact with each other: the errors induced by the discretization scheme can overwhelm the effect of the adopted SGS model for instance. Therefore, the definitions of closure models and numerical schemes are usually carried out simultaneously.

Diversely, in implicit models, not only no filtering operation is performed, but neither an explicit SGS closure model is provided. Instead, the error introduced by the numerical method is modeled in such a way that its dissipation emulates the effect of a SGS term. In this case, the closure model is implicitly introduced by the numerical scheme, considerably reducing the computational cost of the simulation since an explicit computation of the SGS terms becomes unnecessary. This approach is particularly convenient in flow regimes for which the derivation or the accurate computation of explicit SGS models is cumbersome. Many studies performed emphasize the potential of ILES for accurately simulating physically complex geometries and flow configurations.

# Chapter 3

## Methodology

The present thesis activity aims to perform accurate and efficient LES simulations of turbomachinery flow using a research code developed in the Department of Mechanical and Aerospace Engineering (DIMEAS) at the Polytechnic University of Turin by Ferrero, 2015. The code is based on a Discontinuous-Galerkin finite element method implemented in a computationally efficient manner on a modern high performance computing architecture, and it is used to perform a LES of the flow past the T106A rotor passage blade cascade of a LPT. The main features of the method are described in the current chapter, along with the test case configuration and numerical setup.

### 3.1 Discontinuous-Galerkin finite element method

The Discontinuous-Galerkin finite element method was introduced for the first time by Reed and Hill, 1973 and has successfully been implemented recently for the discretization of the Navier-Stokes equations. It combines features of both finite element and finite volume methods. What brings this approach close to the former is the mapping procedure that transfers elements in the physical space to a reference element where the integrals are calculated, while the convective fluxes can be computed with any of the numerical approaches developed in the framework of the finite volume methods. High order reconstructions can be obtained by introducing various degrees of freedom inside the element, thus simplifying the Discontinuous-Galerkin approach with reference to finite volume methods, since all the information required for the integration operation is already inside the element. This aspect considerably alleviates the implementation of the method and renders it highly suitable for efficient parallel computations.

The physical model implemented in the code consists of the Navier-Stokes equations as described by (2.7)-(2.9). To alleviate the problem, these equations are first adimensionalized with respect to the following reference quantities:

- Length  $L_{ref}$
- Pressure  $p_{ref}$

- Temperature  $T_{ref}$
- Density  $\rho_{ref} = \frac{p_{ref}}{RT_{ref}}$
- Velocity  $q_{ref} = \sqrt{RT_{ref}}$
- Time  $t_{ref} = \frac{L_{ref}}{q_{ref}}$
- Energy per mass unit  $E_{ref} = q_{ref}^2$
- Entropy  $s_{ref} = c_v$
- Reynolds number  $Re_{ref} = \frac{\rho_{ref} q_{ref} L_{ref}}{\mu_{ref}}$

and the adimensionalized form is expressed as follows:

$$\frac{\partial \rho}{\partial t} + \frac{\partial \rho u_j}{\partial x_j} = 0 \quad (3.1)$$

$$\frac{\partial \rho u_i}{\partial t} + \frac{\partial \rho u_i u_j}{\partial x_j} + \frac{\partial p}{\partial x_i} = \frac{1}{Re_{ref}} \frac{\partial \sigma_{ij}}{\partial x_j} \quad (3.2)$$

$$\frac{\partial \rho E}{\partial t} + \frac{\partial (\rho E + p) u_j}{\partial x_j} = \frac{1}{Re_{ref}} \frac{\partial \sigma_{ij} u_i}{\partial x_j} - \frac{1}{Re_{ref}} \frac{\partial q_j}{\partial x_j} \quad (3.3)$$

complemented by the non-dimensional perfect gas equation of state:

$$p = \rho T \quad (3.4)$$

Apart from the non-dimensional heat flux that is expressed as:

$$q_j = -\frac{\gamma}{\gamma - 1} \frac{\mu}{Pr} \frac{\partial T}{\partial x_j} \quad (3.5)$$

all the other variables that appear in (3.1)-(3.4) are defined as described in section 2.2.1, except for the fact that they represent non-dimensional quantities.

The Discontinuous-Galerkin finite element method is defined by the variational approach applied to the Navier-Stokes equations system defined in (3.1)-(3.3), which can be expressed in its compact conservative form as:

$$\frac{\partial U}{\partial t} + \nabla \cdot \mathbf{F}(U) = 0 \quad (3.6)$$

where  $U = (\rho, \rho u, \rho v, \rho w, \rho E)^T$  represents the vector of the conservative quantities and  $\mathbf{F}$  is the flux vector field. The latter can be expressed as the difference between the convective and diffusive fluxes:  $\mathbf{F} = \mathbf{G} - \mathbf{H}$ , where:

$$G^i = \begin{pmatrix} \rho u_i \\ \rho u u_i + \delta_{1i} p \\ \rho v u_i + \delta_{2i} p \\ \rho w u_i + \delta_{3i} p \\ (\rho E + p) u_i \end{pmatrix}, \quad H^i = \frac{1}{Re_{ref}} \begin{pmatrix} 0 \\ \sigma_{1i} \\ \sigma_{2i} \\ \sigma_{3i} \\ \sigma_{ij} u_j - q_i \end{pmatrix}, \quad i = 1, 2, 3 \quad (3.7)$$

First of all, the computational domain  $\Omega$  is partitioned into  $N_e$  non-overlapping elements  $\Omega_e$  and the discrete functional space  $V_h$  is defined as:

$$V_h = \{v \in L^3(\Omega) : v|_{\Omega_e} \in P^p(\Omega_e), \forall \Omega_e \in T_h\} \quad (3.8)$$

where  $v$  is a test function,  $P^p$  is the space of polynomials of degree up to  $p$  defined within each element  $\Omega_e$  and  $T_h$  is the ensemble where all the elements  $\Omega_e$  are contained. It is worth noticing that no continuity constraint is applied to the test function, hence the discontinuous nature of the method.

The approximated solution of the conservative quantities  $U$  can be represented by a function  $U_h$ , with  $U_h \in V_h$ . If a basis  $\Phi$  is defined in the functional space containing  $N_e$  basis functions  $\Phi_i$ , the approximated solution can be represented as followed:

$$U_h = \tilde{\mathbf{U}} \cdot \Phi = \sum_{i=1}^{N_e} \tilde{U}_i \Phi_i \quad (3.9)$$

where  $\tilde{\mathbf{U}}$  is the vector containing all the discrete values  $\tilde{U}_i$  of the approximated solution defined at each degree of freedom.

If the exact solution  $U$  in (3.6) is substituted by its approximation  $U_h$ , a residual term that expresses the error of this substitution would appear. According to the Galerkin approach, the projection of the residual on the functional space  $V_h$  equals zero:

$$\int_{\Omega_e} \frac{\partial U_h}{\partial t} v d\Omega + \int_{\Omega_e} \nabla \cdot \mathbf{F}_h v d\Omega = 0, \quad \forall v \in V_h \quad (3.10)$$

and integrating by parts yields:

$$\int_{\Omega_e} \frac{\partial U_h}{\partial t} v d\Omega + \int_{\partial\Omega_e} \mathbf{F}_h^* \cdot \hat{\mathbf{n}} v d\Sigma - \int_{\Omega_e} \mathbf{F}_h \cdot \nabla v d\Omega = 0, \quad \forall v \in V_h \quad (3.11)$$

which is the weak formulation of the method, where the numerical fluxes at the interfaces between adjacent elements  $\mathbf{F}_h^*$  appear.  $\hat{\mathbf{n}}$  represents the outward-pointing unity vector defined at the boundary of the element  $\partial\Omega_e$ .

The condition that equation (3.11) must be satisfied for every test function defined in the functional space is equivalent to setting  $v = \Phi_j$  and imposing that (3.11) is satisfied for all the basis functions. By substituting equation (3.9) in (3.11) and imposing the aforementioned assumption yields:

$$\int_{\Omega_e} \sum_{i=1}^{N_e} \frac{\partial \tilde{U}_i}{\partial t} \Phi_i \Phi_j d\Omega + \int_{\partial\Omega_e} \mathbf{F}_h^* \cdot \hat{\mathbf{n}} \Phi_j d\Sigma - \int_{\Omega_e} \mathbf{F}_h \cdot \nabla \Phi_j d\Omega = 0, \quad 1 \leq j \leq N_e \quad (3.12)$$

Equation (3.12) can be written in the compact form as:

$$[\mathbf{M}] \frac{\partial \tilde{\mathbf{U}}}{\partial t} = -\mathbf{R}(\tilde{\mathbf{U}}) \quad (3.13)$$

where  $[\mathbf{M}]$  is the element mass matrix and  $\mathbf{R}(\tilde{\mathbf{U}})$  is the term regrouping all the flux terms, respectively:

$$[\mathbf{M}]_{ij} = \int_{\Omega_e} \Phi_i \Phi_j d\Omega \quad (3.14)$$

$$\mathbf{R}(\tilde{\mathbf{U}}) = \int_{\partial\Omega_e} \mathbf{F}_h^* \cdot \hat{\mathbf{n}} \Phi d\Sigma - \int_{\Omega_e} \mathbf{F}_h \cdot \nabla \Phi d\Omega \quad (3.15)$$

The choice of the basis function strongly affects the solution accuracy, therefore its definition is not a trivial task. In the present code, an orthonormal element basis is defined according to the modified Gram-Schmidt procedure and following the approach proposed by Bassi et al., 2012.

Different numerical fluxes have been implemented in the code for both convective and diffusive fluxes. The flux solvers used during the thesis activity are the Osher model proposed by Osher and Solomon, 1982 and Pandolfi, 1984 for the convective fluxes, and the Enhanced Stability Recovery (ESR) approach proposed by Ferrero, 2015 for the diffusive ones. Then, the various integrals in (3.14)-(3.15) are approximated through Gauss quadrature formulas defined on the reference element.

An explicit second order two stage Total Variation Diminishing Runge-Kutta (TVD RK) method has been implemented in order to carry out the integration of equation (3.13) through time. A global time stepping strategy is employed according to which the convection and diffusion stability limits are evaluated separately at each iteration and the minimum between the two is chosen as a global time step.

Finally, considering that the aim of the study is to perform a LES simulation on the chosen test case using the Discontinuous-Galerkin method described above, a SGS closure model must also be defined. As described in chapter 2, a closure model is necessary in LES simulations in order to account for the presence of the smallest scales of turbulent motion not represented within the computational grid. This can either be done explicitly by introducing additional terms to the governing equations which produce the necessary dissipation that emulates the effects of the unresolved scales on the resolved ones, or implicitly by adequately adjusting the discretization error produced by the numerical scheme so that it mimics the said dissipation. In the current work an implicit kind of approach was used.

Actually, aside from the superior resolving capabilities and geometric flexibility, Discontinuous-Galerkin methods present some very interesting dispersion and dissipation properties. In a recent work, Gassner and Kopriva, 2011 examined the dispersion and dissipation properties of the Discontinuous-Galerkin spectral element methods for linear wave propagation problems using both Gauss and Gauss-Lobatto quadrature approaches. They stated that the Gauss method was typically more accurate than the Gauss-Lobatto variant. They also showed that the onset of dissipation errors in the former approach moves towards higher wavenumbers with increasing polynomial order as shown in Fig. 3.1. That means that while the polynomial order increases, a wider range of resolved scales are characterized by very small errors, while most of the dissipation occurs at the marginally represented

wavenumbers. Thus, the numerical error of the Discontinuous-Galerkin methods itself behaves as a SGS term.

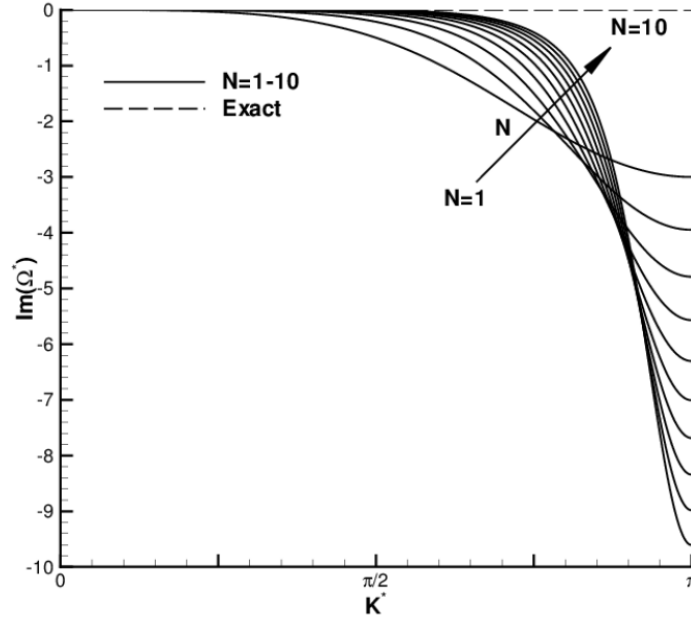


**Figure 3.1:** Dissipation relation of Discontinuous-Galerkin spectral element methods with Gauss nodes, from  $N = 1$  to  $N = 10$ .  $K^* = \frac{K}{N+1}$  is the normalized wavenumber and  $\Omega^*$  is the corresponding modified normalized wavenumber (Gassner and Kopriva, 2011).

These reasons have motivated many researchers to employ Discontinuous-Galerkin methods in order to perform ILES simulations in various study cases. de Wiart and Hillewaert, 2012 and Beck et al., 2014 used this approach to study the transitional flow past the SD7003 airfoil at a moderate Reynolds number, obtaining satisfactory results which accurately matched experimental data and reference DNS numerical results. However, one should point out that the dissipation provided by the Discontinuous-Galerkin discretization scheme error would become insufficient when relatively low resolution computational grids are used and high Reynolds numbers are considered. Thus, explicit SGS modeling becomes necessary.

Taking advantage of the aforementioned characteristics of the Discontinuous-Galerkin approach, in the present study no explicit, nor implicit SGS modeling was performed. Instead, the standard finite element method was used, assuming that the numerical error introduced by the discretization dissipates as a SGS term.

## 3.2 T106A test case description

The test case used for the validation of the available code is the T106A blade profile, which represents the mid section of the Pratt and Whitney PW2037 low pressure turbine rotor passage blade. Many studies have been performed on the said geometry to study boundary layer and other phenomena, such as separation and transition, that characterize typical engine regions with high pressure gradients

and moderate Mach and Reynolds numbers. Many other studies have also been performed in order to explore the effects of wake passing and freestream turbulence on the blade performances.

Stadtmüller et al., 2000 performed various experiments on the T106 blade profile in the High-Speed Cascade Wind Tunnel of the Universität der Bundeswehr München, to investigate wake-induced transition and effects of wake-passing on the boundary layer, also aiming to provide reliable data for the validation of future numerical simulations.

Different configurations of the blade were considered during the experiments, where the acronym T106A stands for design conditions of the blade. While studying the benefits that can be obtained from wake-passing, the pitch-to-chord ratio was increased in order to increase the blade loading. Thus, two more configurations were used, the T106C and T106D, where the pitch-to-chord ratio was set equal to 0.95 and 1.05 respectively, with reference to the design conditions where the pitch-to-chord ratio is set at the value of 0.799.

Experiments were performed with and without wake generators, with very low free-stream turbulence, for different exit isentropic Reynolds and Mach numbers. The upstream stator passage wakes were simulated by a uniformly-spaced bar type wake generator situated in front of the cascade inlet. This setup was denoted as T106A-EIZ, where EIZ indicates the unsteady inflow conditions due to the presence of the bars.

A schematic representation of the apparatus used during the experiments is provided in Fig. 3.2. A seven blade cascade was used and time-resolved and ensemble-averaged hot film data of the blade performances were acquired by measurements performed on the spanwise midsection of the middle blade. This way, it can be assumed that the effects, due to the presence of the cascade tips, on the measurements are negligible. Wake losses were also measured at a distance 40% of the chord length downstream the cascade exit plane, using a fast-response wake rake paired with conventional Pitot probes.

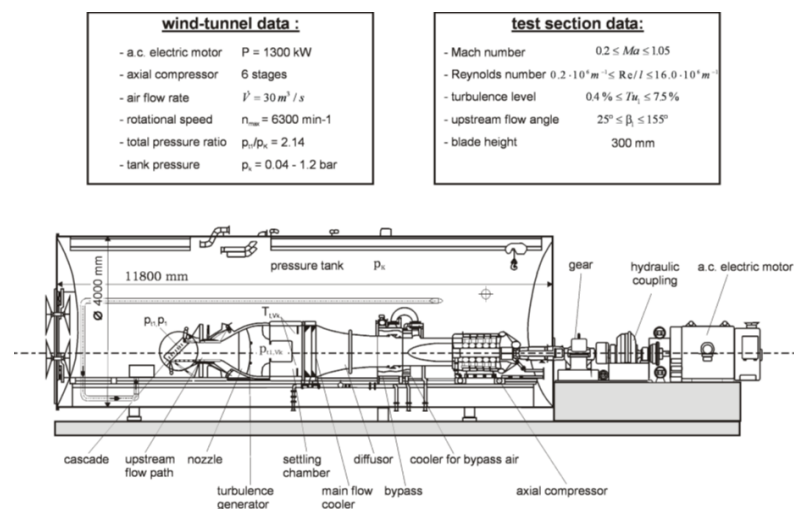


**Figure 3.2:** High-Speed Cascade Wind Tunnel of the Universität der Bundeswehr München (Stadtmüller et al., 2000).

The blade aspect ratio  $h/C$  used during the experiments is 1.76. This value allows to assume the flow field to be statistically two-dimensional in the spanwise midsection, that is the spanwise direction can be treated as a statistically homogeneous direction. Uncertainties regarding the correct value of the geometric inlet angle  $\beta_1$  have risen due to the flow leakage through small gaps positioned at the top and the bottom ends of the wind tunnel. These gaps were present in order to enable the periodic movements of the wake generator belt inside the experiment chamber.

With the available experimental data provided by [Stadtmüller et al., 2000](#), various numerical studies on the T106A turbine blade were performed by many researchers. One of the first studies was the incompressible DNS performed by [Wissink, 2003](#) to study the effects of wake-passing. More recently, [R. Sandberg et al., 2012](#) and [Michelassi et al., 2015](#) used compressible DNS to investigate the effects of inflow disturbances on the transition and wake regions of the blade. [Garai et al., 2015](#) used the T106A configuration with "clean" and steady inflow conditions, thus with no freestream turbulence and no wake generator, to validate their code based on an entropy-stable Discontinuous-Galerkin spectral element method.

In the current work, a LES is conducted on the T106A configuration without freestream turbulence ( $FSTI = 0\%$ ) and with steady inflow boundary conditions, for the reference operating point with  $Re_{2,is} = 60000$  and  $M_{2,is} = 0.4$ . Both numbers refer to the exit isentropic velocity  $q_{2,is}$  and the airfoil chord  $C$ . The geometry of the blade airfoil is represented in Fig. 3.3. The pitch-to-chord ratio is set to its design conditions:  $t/C = 0.799$ . The stagger angle  $\gamma$  and geometric inlet angle  $\beta_1$  are  $30.72^\circ$  and  $37.7^\circ$  respectively. All angles are defined with respect to the axial direction.

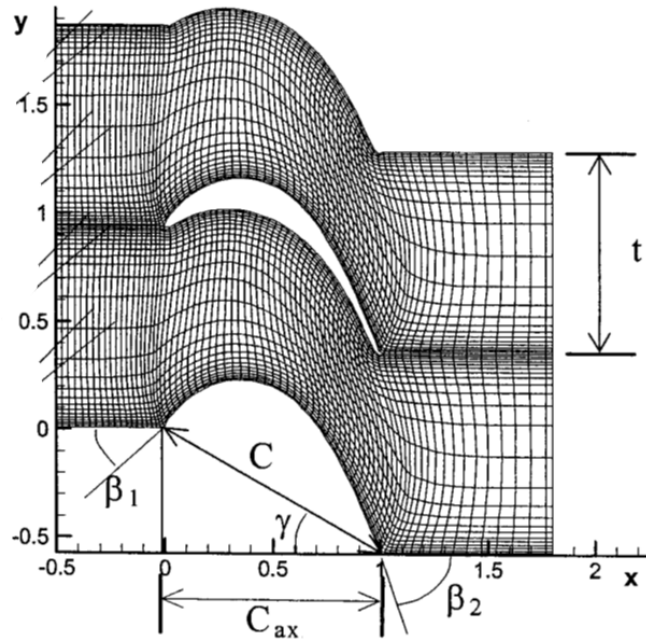


**Figure 3.3:** T106A blade airfoil geometry ([Michelassi et al., 2015](#)).

To overcome the uncertainties characterizing the geometric inlet angle  $\beta_1$ , [Stadtmüller et al., 2000](#) performed RANS simulations at different geometric inflow angles in order to evaluate the best numerical match with the experimental data. This was obtained for  $\beta_1 = 45.5^\circ$ , whereas [R. Sandberg et al., 2012](#) DNS simulations suggest a slightly different value:  $\beta_1 = 46.1^\circ$ , for which their DNS perfectly matched with the experimental data. In the present study, the second value of  $46.1^\circ$  was considered.

The experimental data provided by [Stadtmüller et al., 2000](#), for the same configuration and operating point, were used in order to validate the results provided by the code with reference to time-averaged wake losses profile. A further comparison with numerical data from [Garai et al., 2015](#) DNS simulation is made. The total pressure losses in the wake are evaluated on a control station surface along the pitchwise direction, situated at a distance 40% of the chord length from cascade exit plane:  $d_m/C = 0.4$ . The parameters used during the study defining the test case configuration are summarized in Tab. 3.1.

**Table 3.1:** Parameters defining the T106A test case configuration .

Parameter	Value
Stagger angle $\gamma$	$30.72^\circ$
Geometric inlet angle $\beta_1$	$46.1^\circ$
Pitch-to-chord ratio $t/C$	0.799
Measurement plane $d_m/C$	0.4
Exit isentropic Reynolds number $Re_{2,is}$	60000
Exit isentropic Mach number $M_{2,is}$	0.4
Static pressure at the outlet $p_2/p_{t1}$	0.8956

### 3.3 Mesh generation

As mentioned in the previous chapter, the blade aspect ratio is sufficiently high so that any eventual disturbances, arising from the presence of the cascade casing, do not reach the blade midspan section. This allows to consider the flow to be statistically two-dimensional at the midspan section. Even though phenomena such as tip clearance, or boundary layers at the cascade's casing are of important nature, they will not be treated in the current work. Thus, their presence will not be taken into account in the computational domain and consequently the spanwise direction can be treated as a statistically homogeneous direction, equivalent to considering an infinite aspect ratio.

For this reason, the unstructured mesh, generated on Gmsh, is created by firstly constructing a 2D mesh on the blade's airfoil plane  $x - y$  (Fig. 3.4) and then extruding it along the spanwise direction  $z$  (Fig. 3.5). The spanwise extension of the grid is set to:  $\frac{h_g}{C_{ax}} = 0.2$ , where  $h_g$  is the extrusion parameter and  $C_{ax}$  is the

axial chord, and 20 layers of elements are used for the extrusion. Reference studies show that this value of the mesh spanwise extent is deemed to be sufficient in order to capture the largest vortices along the third direction.

The Cartesian reference system is centered at the leading edge, even though it is translated in Fig. 3.4 and Fig. 3.5 in order to have a clearer representation. The three axis  $x$ ,  $y$  and  $z$  represent the three directions streamwise, pitchwise and spanwise respectively. The coordinates of the blade profile are generated in such a way that  $C_{ax} = 1$ .

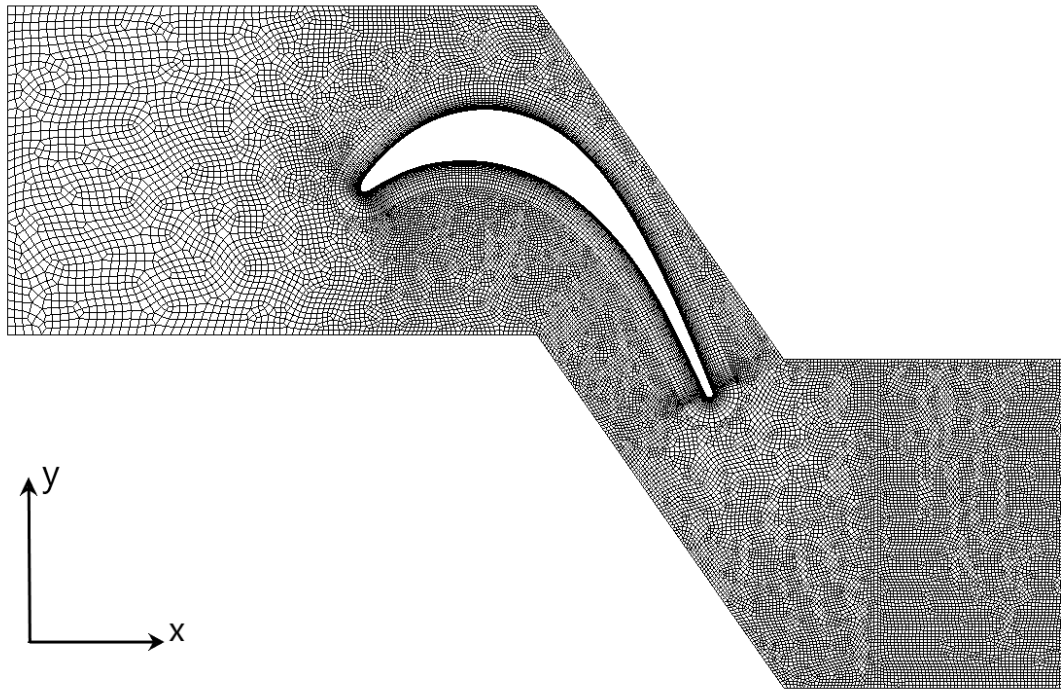


**Figure 3.4:** 2D mesh generated with Gmsh.

Moreover, the inflow and outflow boundaries of the computational domain are located at a distance of one axial chord length  $C_{ax}$  from the Leading Edge (LE) and the Trailing Edge (TE) respectively. These distances are deemed to be sufficient so that the inflow conditions do not interfere with the blade inlet plane and in order to be able to capture the most energetic part of the wake. The pitch-to-chord ratio is set to:  $t/C = 0.799$  and the control station surface, where the wake losses are measured, is located at  $40\%C$  distance downstream from the cascade exit plane:  $d_m/C = 0.4$ .

It should be highlighted that near solid wall regions, even the most dominant scales are too small in size. Therefore, in order to accurately solve these regions, mesh resolution must increase while getting nearer to the wall. To do so, a structured O-type mesh is generated around the blade profile, whereas the grid is unstructured elsewhere. This also enables an adequate mesh resolution at the LE and TE which is very important, since highly deformed elements in these two zones would compromise the stability of the numerical method.

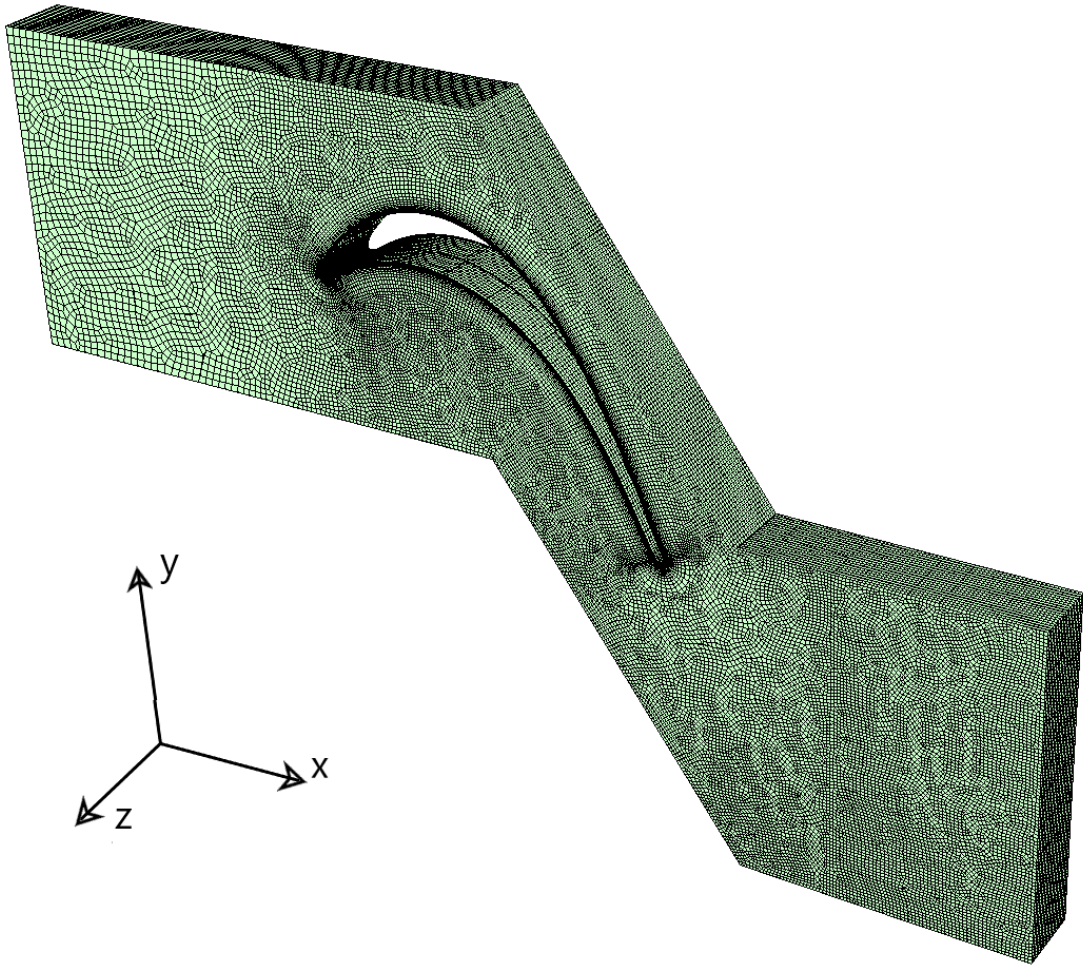


**Figure 3.5:** 3D mesh generated with Gmsh.

For the implementation of the previously mentioned aspect, a boundary layer field is defined around the blade's solid wall. The thickness of the field is set to  $0.08C_{ax}$  measured on the wall normal direction, while the element size growth rate along this direction is set to 1.2.

In order to adequately refine the mesh, attractor and threshold fields are defined. The idea between attractors and thresholds is that the former return the distance to a given entity and the latter use the return value of the attractor in order to define a simple change in element size around the given entity. Attractor and threshold fields are defined at the blade wall boundary, at the LE and TE, at the control station and at the outflow plane. Then, the minimum value of all fields is used as a background field for the whole domain. In order to save in computational costs, no attractor is applied at the inlet, since no freestream turbulence is considered and thereby no particularly high resolution is required.

It is also important that after the meshing process, the control surface results in a plane surface. This is done by defining two separate volume entities while building the geometry, so that they interface exactly at the control station plane.

Finally, the code is implemented in such a way that it can only deal with hexahedral 3D elements. Since the grid generation consists in extruding the 2D

mesh along the spanwise direction, then the 2D elements define the type of the generated 3D elements. Thus, a fully quadrilateral 2D mesh is required and this can be obtained with a Frontal-Delaunay algorithm for the 2D mesh generation, and a Blossom algorithm for the 2D recombination of triangular elements into quadrilateral ones. After the meshing process,  $N_e = 511060$  3D hexahedral elements are generated.

### 3.4 Flow and boundary conditions

The boundary conditions must be defined in order to obtain a well posed problem. The implemented boundary conditions are represented in Fig. 3.6. A no-slip adiabatic condition is imposed at the solid wall and periodic conditions in the pitchwise direction. This is somehow reasonable considering the blade is part of a cascade, where other blades are replicated uniformly. Many studies have imposed periodic boundary conditions along the spanwise direction too, justifying their choice by the statistically homogeneous character of the latter. The current version of the code, however, can only deal with one direction of periodicity, therefore tangency conditions are imposed at the spanwise boundaries.

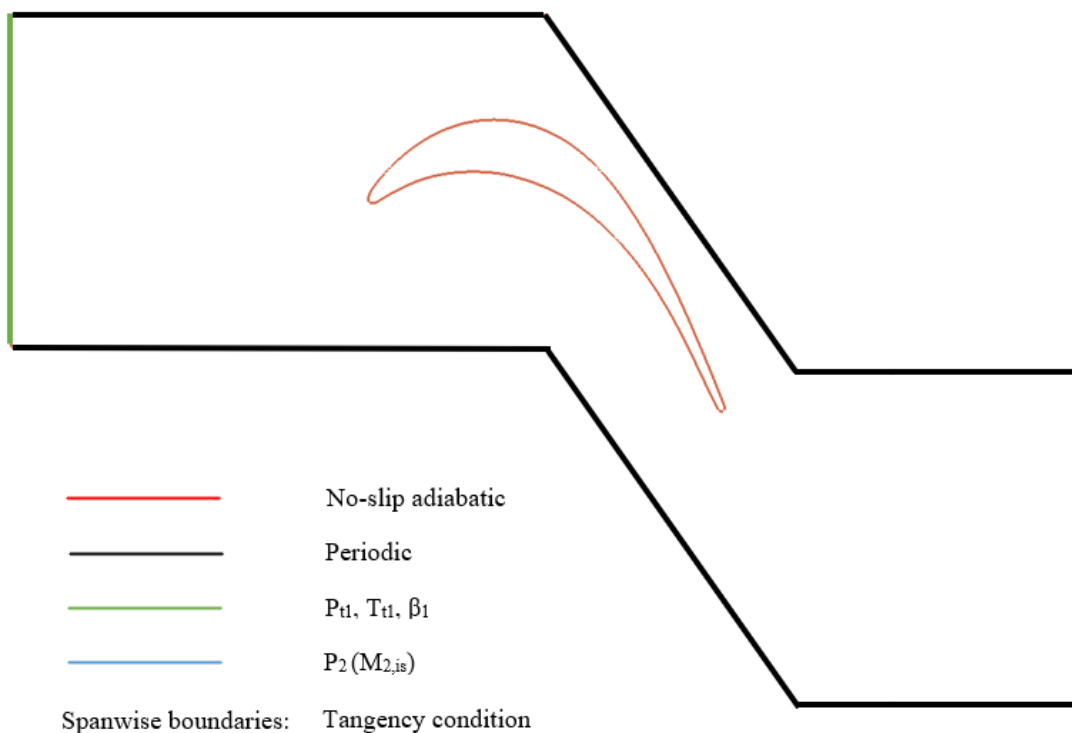


**Figure 3.6:** Imposed boundary conditions for numerical computation.

Moreover, three parameters are assigned at the inflow boundary: total temperature  $T_{t1} = 1$ , total pressure  $p_{t1} = 1$ , and the inlet geometric angle  $\beta_1 = 46.1^\circ$ . The values of the first two parameters are non-dimensional and since they are unity, this means that total temperature and total pressure at the inlet are used to

adimensionalize the Navier-Stokes equations. Static pressure is the only parameter assigned at the outflow boundary, which is equivalent at imposing the exit isentropic Mach number  $M_{2,is}$ , considering that:

$$\frac{p_2}{p_{t1}} = \frac{1}{\left(1 + \frac{\gamma-1}{2} M_{2,is}^2\right)^{\frac{\gamma}{\gamma-1}}} \quad (3.16)$$

Since  $M_{2,is} = 0.4$ , then the ratio  $\frac{p_2}{p_{t1}} = 0.8956$ .

In order to conclude, the considered test case configuration is characterized by a moderate exit isentropic Reynolds number:  $Re_{2,is} = \frac{\rho_{2,is} q_{2,is} C}{\mu} = 60000$ . The isentropic expansion factor  $\gamma$ , the Prandtl number  $Pr$  and the dynamic viscosity  $\mu$  are considered to be constant. Following its definition:  $\lambda = \frac{\mu C_p}{Pr}$ , the thermal conductivity is also constant. For air:  $\gamma = 1.4$ ,  $Pr = 0.72$  and the non-dimensional value of the dynamic viscosity is set to  $\mu = 1$ , while the reference value used for adimensionalization is:  $\mu_{ref} = 9.3 \cdot 10^{-6} Pa \cdot s$ .

### 3.5 Parallel work

The local nature of the Discontinuous-Galerkin approach makes this method a viable candidate for parallel implementation. The code used during the present thesis activity is written in FORTRAN and is parallelized by means of standard Message Passing Interface (MPI) libraries.

The Portable, Extensible Toolkit for Scientific Computation (PETSc) software is used to carry out the parallelization of the computational grid. The mesh partitioning is performed using the DMPlex module of the PETSc libraries. The mesh is subdivided into many subdomains, one for each processor used during the parallel computation. A layer of ghost cells at the interfaces of each subdomain is created and by means of MPI, different processors communicate between them. Data is exchanged and saved inside the ghost layers. No interactive action with the user is required, since the parallelization is completely carried out autonomously by PETSc and its modules, while the communication between different processors is made possible using MPI libraries.

Finally, the simulations were carried out using computational resources provided by HPC@POLITO, which is a project of Academic Computing within the Department of Control and Computer Engineering at the Polytechnic University of Turin. Computations were performed on the Legion cluster, which comprises of 2x Intel Xeon Scalable Processors Gold 6130 2.10 GHz 16 cores per node.

# Chapter 4

## Numerical results

The main goal of the present thesis is to validate the code described in the previous chapter on the turbulent transitional flow past the T106A blade cascade. To this purpose, two LES simulations were performed using a second order approximation in time and second and third order approximations in space. Both simulations were carried out in parallel on the Legion cluster using 8 nodes with 32 cores per node, thereby resulting in a total of 256 processes.

Instantaneous data is provided for both simulations in terms of Mach and spanwise vorticity fields at the midspan section and the solution resolution obtained is compared to reference DNS numerical data provided by [Garai et al., 2015](#). Instantaneous isosurfaces of entropy and second invariant of the velocity gradient tensor (Q-criterion) are used instead for the visualization of the vortical structures that form in the wake. Aside to instantaneous results, time- and spanwise-averaged data in terms of total pressure losses in the wake are also provided for a further comparison with experimental data presented by [Stadtmüller et al., 2000](#).

Results show that better solution resolution is obtained with increasing order. However, both second and third order simulations fail to accurately predict wake losses profile.

### 4.1 Simulations setup

It is common in literature to refer to convective time units. A convective time is here defined as the ratio between the non-dimensional chord length and exit isentropic velocity, which are expressed as follows:

$$C = \frac{C_{ax}}{\cos \gamma} \approx 1.1632 \quad (4.1)$$

$$q_{2,is} = M_{2,is} \sqrt{\frac{\gamma}{1 + \frac{\gamma-1}{2} M_{2,is}^2}} \approx 0.4659 \quad (4.2)$$

therefore, one convective time is:

$$t_c = \frac{C}{q_{2,is}} \approx 2.5 \quad (4.3)$$

At first, a second order simulation was initialized by using Lax-Friedrichs solver for the convective fluxes, which is a very dissipative method with reference to the Osher solver, especially for low approximation orders. Indeed, in this case the vortices were strongly two-dimensional and they didn't "break" along the spanwise direction. After several convective times, the Osher flux solver was activated and two separate simulations, of second and third order, were let to evolve from here.

In order to evaluate whether the two solutions had statistically converged, the evolution of force coefficients of the blade over time was studied. Since by definition a LES simulation is inherently unsteady, we cannot expect for instantaneous solutions to converge. However, considering time is a statistically homogeneous direction, one expects that mean values of flow field quantities would converge to a statistically asymptotic solution.

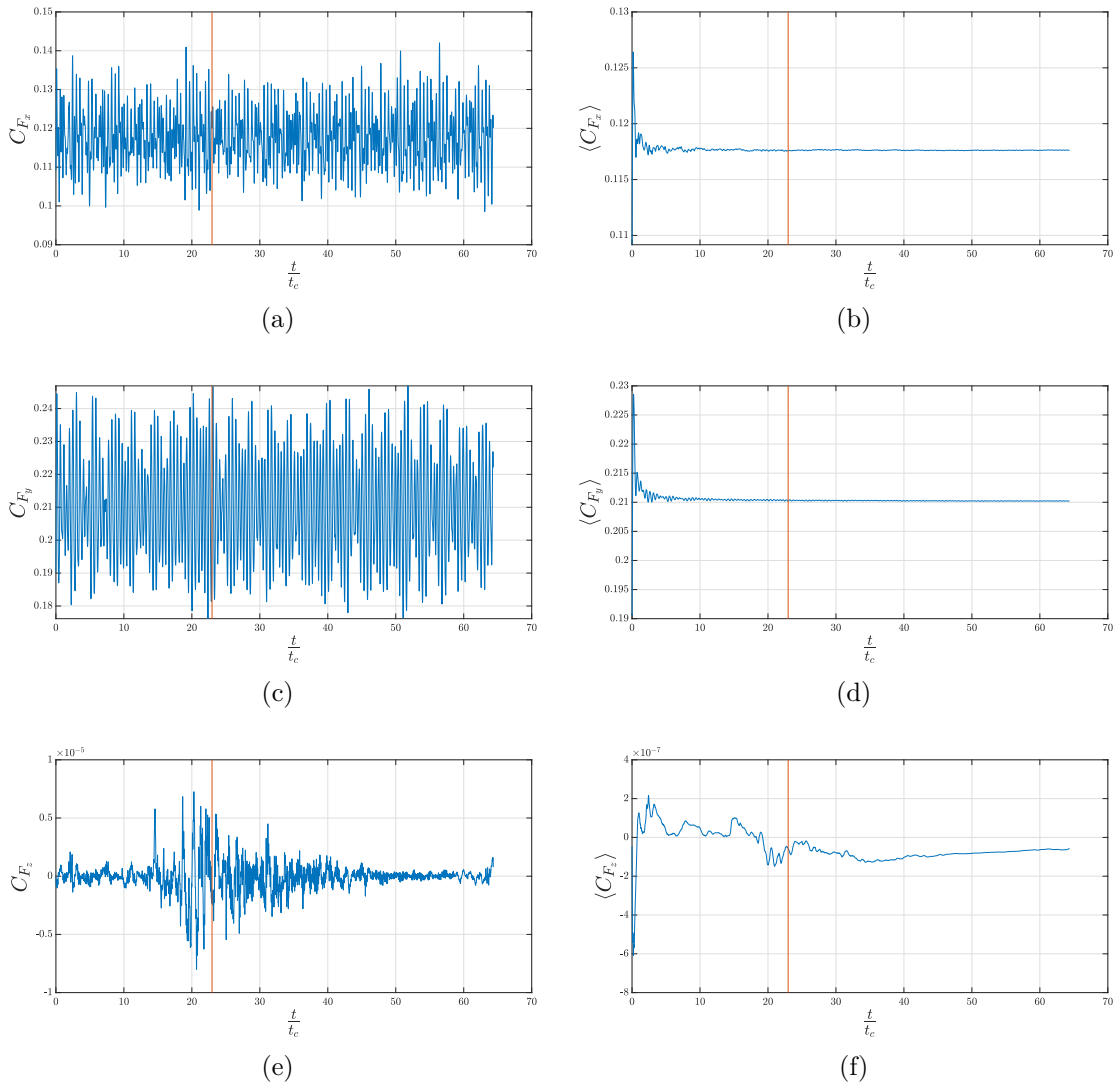


**Figure 4.1:** Force coefficients evolution over time for second order simulation: Instantaneous values on the left and mean values on the right. The red line denotes the separation between discarded convective times and those used for the averaging process of the data.

Fig. 4.1 represents the evolution in time of the instantaneous values of blade force coefficients on the left side, and the evolution in time of the mean values of the coefficients on the right side for the second order simulation. It can be noticed how instantaneous values are continuously oscillating, while the mean values converge towards an asymptotic solution after a few convective times. The initial instant represents the moment in which the flux solvers were switched. One can also notice how the mean force coefficients along the streamwise and pitchwise directions tend to approximately 0.118 and 0.21 respectively, while the force coefficient along the spanwise direction is clearly negligible since the oscillations are of the order of  $10^{-7}$ .

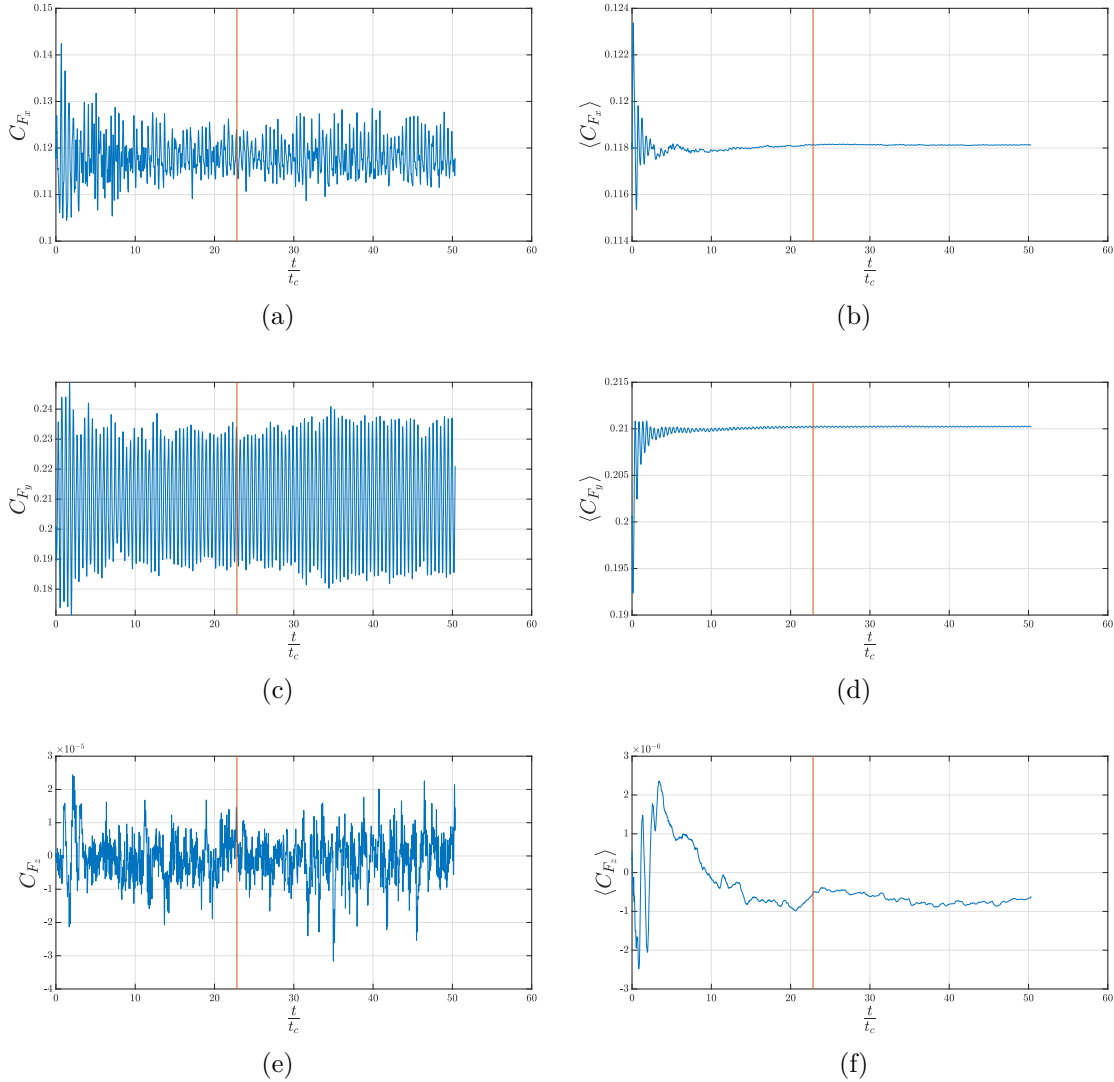


**Figure 4.2:** Force coefficients evolution over time for third order simulation: Instantaneous values on the left and mean values on the right. The red line denotes the separation between discarded convective times and those used for the averaging process of the data.

Analogous considerations can be made for the third order simulation. Similarly to the second order, Fig. 4.2 provides the evolution over time of instantaneous and

mean values of the force coefficients for the third order. One can notice that both  $C_{F_x}$  and  $C_{F_y}$  statistically converge towards the same values as in the second order, while  $C_{F_z}$  is still negligible.

The condition in which the solution can be retained as statistically converged is important especially when time-averaged data are to be calculated. In both simulations, the red line denotes the moment in which both solutions can be considered as statistically stationary. This happens at approximately 22 convective times. So, the time-averaging process for wake losses profile was started after 22 convective times and was performed over an interval of approximately 40 convective times for the second order simulation and 28 for the third order.

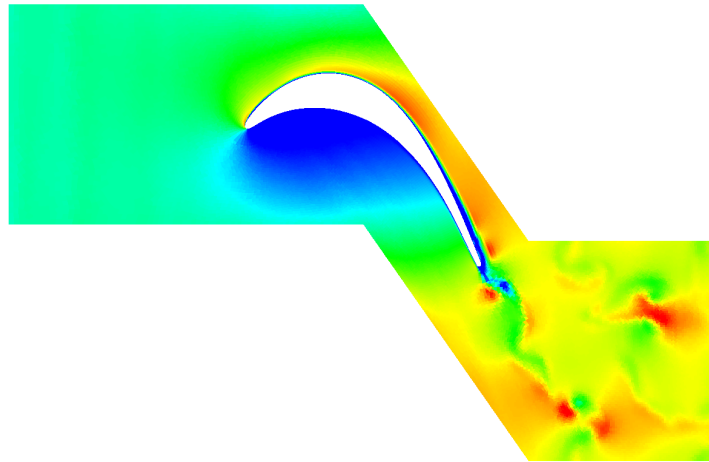
The intention was to perform the time-averaging process of the data over the same length of time interval for both simulations, but there is a 10 day time-limit for every job performed in the HPC@POLITO clusters and since the third order simulation was considerably slower than the second order, it reached the time-limit without covering all 40 convective times.

## 4.2 Flow visualization

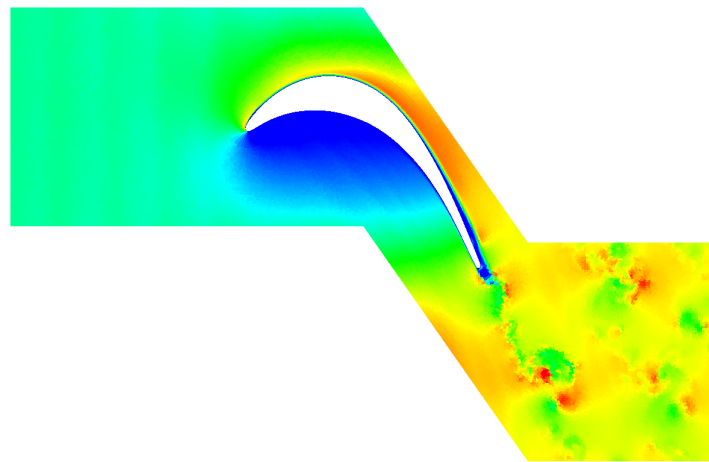
In Fig. 4.3, instantaneous Mach fields at the blade midspan section are shown for second and third order simulations along with the instantaneous velocity magnitude field for the reference DNS simulation. It can be noticed how the resolution of the flow field increases with increasing approximation order. Both methods seem to accurately capture the main aspects of the flow. There is a stagnation point at the vicinity of the LE and the flow remains laminar in the pressure side and in the fore region of the suction side. On the aft region of the latter, separation and transition occur and afterwards the flow becomes fully turbulent downstream.

Uncertainties on the experimental data provided by [Stadtmüller et al., 2000](#) occur on whether an open or closed separation bubble is formed. In order to predict the accurate position of the separation and the transition position and length, time-averaged data of blade performances are needed, that is blade loading and skin friction coefficient. However, the current version of the code was able to provide only instantaneous data for the said quantities, thereby not allowing a possible comparison with the experimental data.

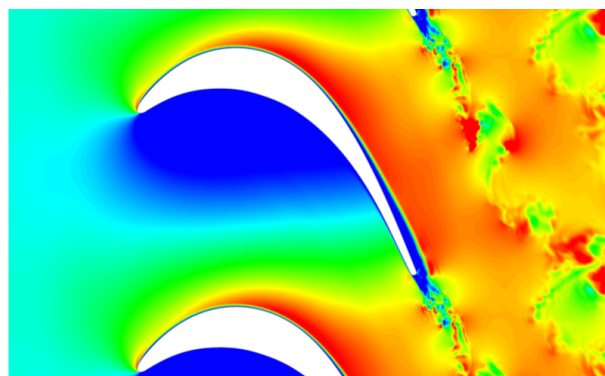
Moreover, the resolution difference between the two different approximation orders can especially be noticed in the spanwise vorticity field visualizations at the midspan section (Fig. 4.4). The second order simulation is able to represent only a limited range of scales of the turbulent motion, whereas due to the higher resolution capabilities of the third order scheme, smaller scales can be captured by the method.



(a) Second order simulation

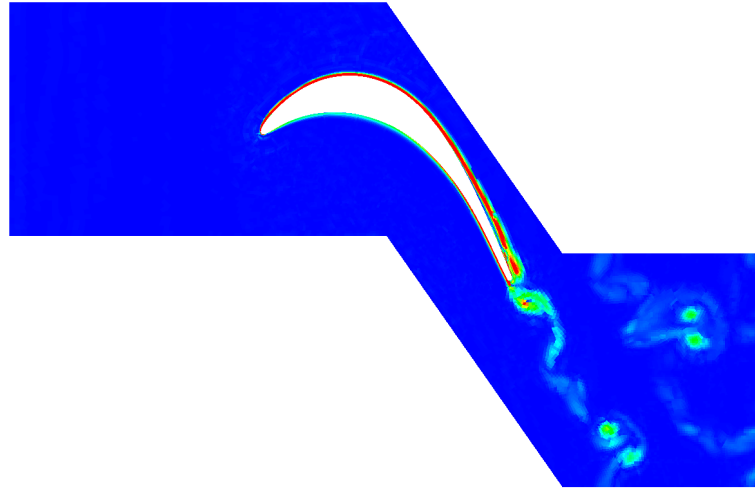


(b) Third order simulation

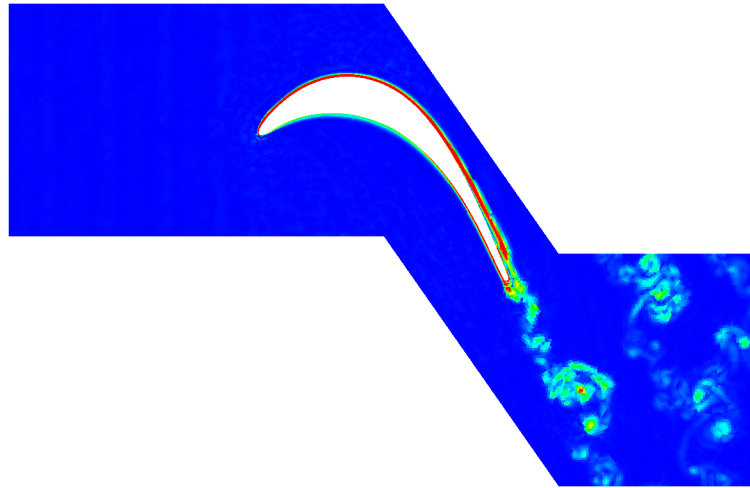


(c) Reference DNS

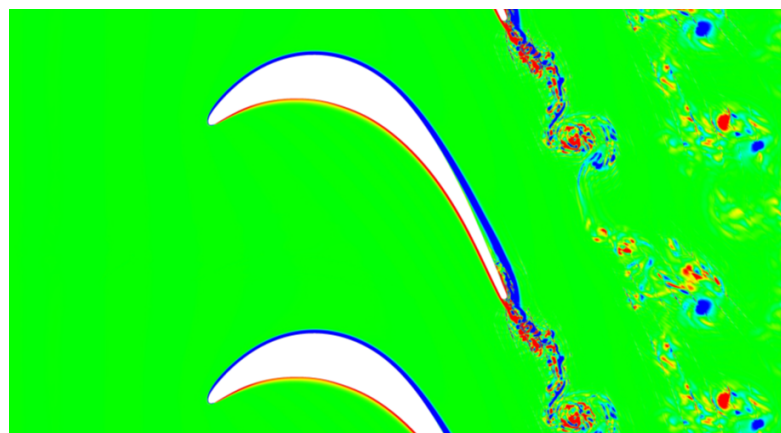
**Figure 4.3:** Instantaneous Mach field visualizations at the midspan section for: (a) second order simulation and (b) third order simulation. Instantaneous velocity magnitude field at the midspan section for (c) reference DNS (Garai et al., 2015).



(a) Second order simulation



(b) Third order simulation



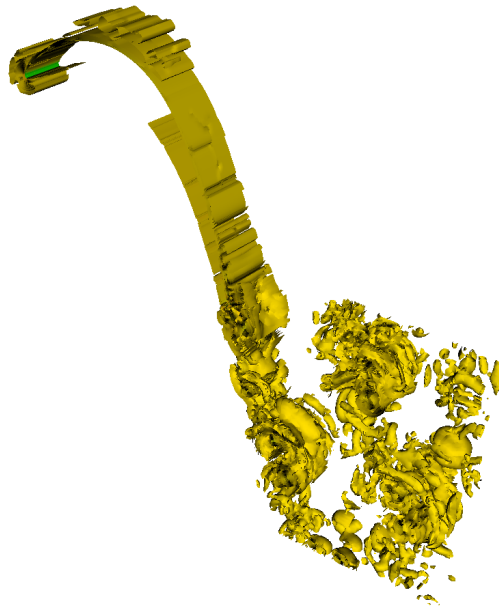
(c) Reference DNS

**Figure 4.4:** Instantaneous spanwise vorticity fields at the midspan section for: (a) second order simulation, (b) third order simulation and (c) reference DNS (Garai et al., 2015).

For a better visualization of the vortex shedding that occurs in the aft region of the suction surface, the second invariant of the velocity gradient tensor, or Q-criterion, can be considered. It has been proven to be effective in highlighting coherent vortical structures (Dubief and Delcayre, 2000).



(a) Second order simulation

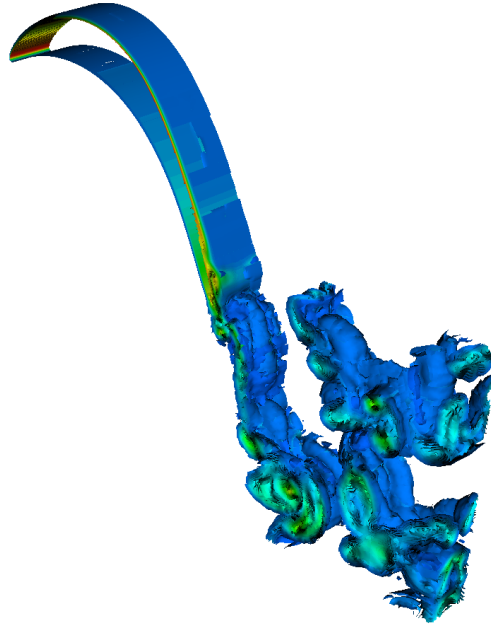


(b) Third order simulation

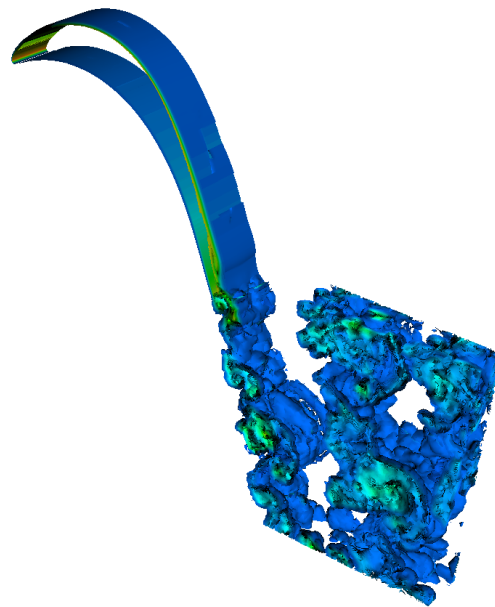
**Figure 4.5:** Isosurfaces of instantaneous second invariant of the velocity gradient tensor (Q-criterion) for: (a) second order simulation and (b) third order simulation.

In Fig. 4.5 isosurfaces of the Q-criterion for  $N = 900$  levels are represented for both simulations. It can be noticed how the flow remains laminar along most

of the length of the suction surface. The dead air area that is created in the aft region of the suction surface due to the separation, pushes the separated laminar boundary layer away from the blade surface. The separated shear layer then rolls up and breaks down into complex three-dimensional structures further downstream. Once again, a better visualization is obtained with a higher order, which is able to capture much smaller eddies with respect to the second order scheme.



(a) Second order simulation



(b) Third order simulation

**Figure 4.6:** Isosurfaces of instantaneous entropy field for: (a) second order simulation and (b) third order simulation.

An alternative way of visualizing the turbulence structures in the wake is by plotting isosurfaces of the entropy field as represented in Fig. 4.6 for  $N = 100$  levels. It gives a very clear representation of the fully turbulent structure of the wake, even though the vortical structures are strongly coupled with each other, in contrary to the visualization provided by the Q-criterion tensor characterized by a clearer separation of the three-dimensional structures of the vortices.

### 4.3 Wake losses profile

A further validation of the code is provided by the time-averaged losses profile in the wake. In the experimental work performed by Stadtmüller et al., 2000, the total pressure losses in the wake are measured in a control surface situated at a distance of  $40\%C$  downstream of the cascade exit plane (Fig. 4.7). The losses are expressed in terms of the wake deficit coefficient and they are plotted along the pitchwise direction normalized by the blade's pitch, starting from the suction side towards the pressure side. However, there is no precise indication on the exact measurement position along the control surface.

In the present work, the time-averaging process was started 22 convective times after the flux solver switch and was performed over an interval of 40 convective times for the second order scheme and 28 for the third order one. Moreover, considering the spanwise direction is statistically homogeneous, the time-averaged data can further be averaged along the spanwise direction. As far as the measurement position along the control surface is concerned, the origin of the reference system is placed at the intersection between the streamwise axis direction and the control surface. This is justified by the fact that this approach was adopted by Stadtmüller in further experiments performed on the T106C blade cascade.

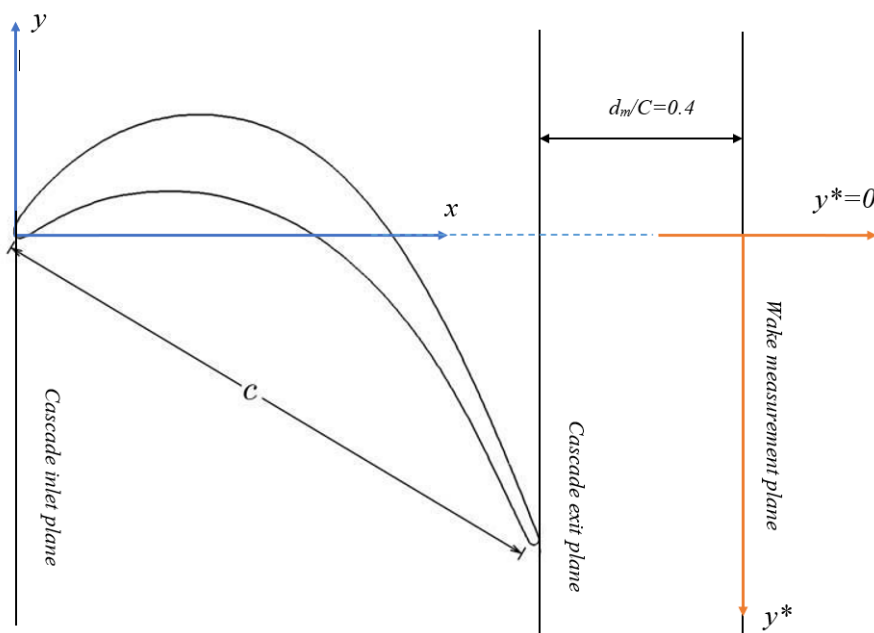


Figure 4.7: Wake measurement plane.

The wake deficit coefficient is then defined:

$$\xi(y^*) = \frac{p_{t1} - p_t(y^*)}{p_{t1} - p_2} = \frac{1 - \frac{p_t(y^*)}{p_{t1}}}{1 - \frac{p_2}{p_{t1}}} \quad (4.4)$$

and the normalized pitchwise direction is expressed as:

$$y^* = -\frac{y}{t} \quad (4.5)$$

The numerical results provided by the code for the second and third order simulations are presented in Fig. 4.8 and compared to the experimental data of [Stadtmüller et al., 2000](#) and DNS numerical results of [Garai et al., 2015](#). Both simulations fail to accurately predict the wake profile losses, by underestimating the peak total pressure drop in the wake. The reference system adopted along the pitchwise direction seems to be suitable for the third order simulation and the latter moderately approximates the wake width. The second order simulation solution, on the other hand, is shifted towards the suction side.

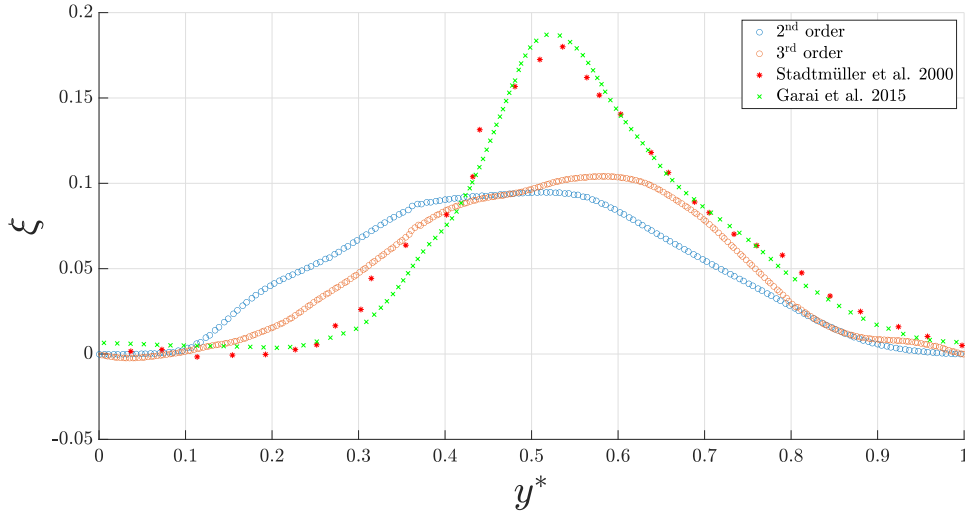


**Figure 4.8:** Wake loss coefficient profile for second and third order simulations, compared to experimental data ([Stadtmüller et al., 2000](#)) and reference DNS ([Garai et al., 2015](#)). The values refer to time- and spanwise-averaged total pressure losses in the wake, measured on a plane  $40\%C$  downstream from the cascade exit.

These errors might be traced to insufficient resolution for both methods. Even though the third order simulation is able to capture in a more accurate way some of the physical aspects of the flow field with reference to the second order scheme, still the errors represented by the method do not accurately represent the SGS effects. Therefore, higher order must be considered in order to reach higher resolutions in the solution and better agreements with the experimental data

# Chapter 5

## Conclusions

In the current work, investigation of turbulent transitional flow past the T106A blade cascade of a LPT is performed, using a LES simulation by means of a code based a Discontinuous-Galerkin finite element method. The code is implemented in a computationally efficient manner on a modern high performance computing center.

At first, a general overview on the most diffused simulation methods for turbulent flows is provided, with a highlight on the LES approach. The superior resolution capabilities of LES over RANS models, along with the lower computational cost with respect to DNS, make this method a viable candidate for studying complex geometries and flow configurations. However, many important issues that the method presents have to be overcome in order for the LES approach to become a routine basis analysis tool in the engineering field and completely substitute RANS models.

A second part of the thesis addresses the theoretical aspect of the LES approach, with emphasis on the derivation of a mathematical model and turbulence closure methods. Firstly, the Kolmogorov's theory of the energy cascade for homogeneous and isotropic turbulence is introduced, in order to point out the lack of generality of these simplified theories and their incapability to predict complex flows, thus identifying the great need for accurate high-fidelity numerical approaches. Afterwards, the convolution filtering approach is introduced and the filtered governing equations are derived, concluding with a brief description of the current state-of-the-art for SGS modeling.

Furthermore, an insight on the Discontinuous-Galerkin finite element method is provided, along with the description of the validation test case considered and its numerical setup. The very interesting dispersion and dissipative properties of the Discontinuous-Galerkin approach allow for the employment of this method to conduct implicit LES simulations. By avoiding the implementation and computation of a SGS model, the computational cost is reduced. However, for low resolution grids and for high Reynolds numbers, the numerical dissipation of these methods is deemed to be insufficient in order to accurately represent a SGS term. Therefore, in these cases an explicit turbulence model is required. However, this method presents very low numerical errors and its local nature allows for an efficient parallelization, with a consequent reduction in computational time. These properties also allow for

the Discontinuous-Galerkin approach to be employed in very complex geometries and flow configurations.

Finally, the code based on the Discontinuous-Galerkin finite element method is used to conduct a LES on the T106A blade cascade. Two simulations were carried out, with second order approximation in time and second and third order approximations in space. The numerical results for both simulations are reported and confronted with the available experimental data and other reference numerical results. The method is able to capture the main physical aspects of the flow. However, time-averaged data of blade performances are required, in order to predict and confront the exact position of separation and transition position and length with the reference data. Moreover, both simulations fail to predict the correct time-averaged wake losses profile, by underestimating the peak pressure loss in the wake. The third order simulation seems to accurately capture the wake width, while second order method is shifted towards the suction side. In order to increase the solution resolution, higher order simulations must be conducted.

# Bibliography

Sandberg, Richard D and Vittorio Michelassi

- 2019 ‘The current state of high-fidelity simulations for main gas path turbomachinery components and their industrial impact’, *Flow, Turbulence and Combustion*, 102, 4, pp. 797-848. (Cit. on p. 1.)

Gerretsen, John C and Rainer Kurz

- 2009 ‘Powering progress with clean gas turbine systems’, *Solar Turbines Incorporated*. (Cit. on p. 1.)

Pope, Stephen B

- 2001 *Turbulent flows*. (Cit. on pp. 2, 4, 11, 14, 22.)

Garai, Anirban, Laslo Diosady, Scott Murman, and Nateri Madavan

- 2015 ‘DNS of flow in a low-pressure turbine cascade using a discontinuous-galerkin spectral-element method’, in *Turbo Expo: Power for Land, Sea, and Air*, American Society of Mechanical Engineers, vol. 56642, V02BT39A023. (Cit. on pp. 2, 33, 34, 39, 43, 44, 48.)

Babajee, Jayson

- 2013 *Detailed numerical characterization of the separation-induced transition, including bursting, in a low-pressure turbine environment*, PhD thesis. (Cit. on pp. 3, 4.)

Hourmouziadis, Jean

- 1989 ‘Aerodynamic design of low pressure turbines’, *AGARD, Blading Design for Axial Turbomachines 40 p(SEE N 89-27661 22-07)*. (Cit. on pp. 3, 4.)

Fröhlich, J and W Rodi

- 2002 *Introduction to large eddy simulation of turbulent flows*. (Cit. on pp. 5, 18.)

De Wiart, C Carton and K Hillewaert

- 2012 ‘DNS and ILES of transitional flows around a SD7003 using a high order discontinuous Galerkin method’, in *Seventh international conference on computational fluid dynamics (ICCFD7)*, Big Island, Hawaii. (Cit. on pp. 5, 31.)

- Fröhlich, Jochen and Dominic Von Terzi  
2008 ‘Hybrid LES/RANS methods for the simulation of turbulent flows’, *Progress in Aerospace Sciences*, 44, 5, pp. 349-377. (Cit. on p. 6.)
- Piomelli, Ugo and Elias Balaras  
2002 ‘Wall-layer models for large-eddy simulations’, *Annual review of fluid mechanics*, 34, 1, pp. 349-374. (Cit. on p. 6.)
- Deck, Sébastien, Fabien Gand, Vincent Brunet, and Saloua Ben Khelil  
2014 ‘High-fidelity simulations of unsteady civil aircraft aerodynamics: stakes and perspectives. Application of zonal detached eddy simulation’, *Philosophical Transactions of the Royal Society A: Mathematical, Physical and Engineering Sciences*, 372, 2022, p. 20130325. (Cit. on p. 6.)
- Smagorinsky, Joseph  
1963 ‘General circulation experiments with the primitive equations: I. The basic experiment’, *Monthly weather review*, 91, 3, pp. 99-164. (Cit. on pp. 6, 24.)
- Deardorff, James W et al.  
1970 ‘A numerical study of three-dimensional turbulent channel flow at large Reynolds numbers’, *J. Fluid Mech*, 41, 2, pp. 453-480. (Cit. on p. 6.)
- Zhiyin, Yang  
2015 ‘Large-eddy simulation: Past, present and the future’, *Chinese journal of Aeronautics*, 28, 1, pp. 11-24. (Cit. on p. 7.)
- Garnier, Eric, Nikolaus Adams, and Pierre Sagaut  
2009 *Large eddy simulation for compressible flows*, Springer Science & Business Media. (Cit. on pp. 7, 9, 12, 14, 21, 23.)
- Tyacke, James C and Paul G Tucker  
2015 ‘Future use of large eddy simulation in aero-engines’, *Journal of Turbomachinery*, 137, 8. (Cit. on p. 7.)
- Ferrero, Andrea  
2015 *Computational fluid dynamics for aerospace propulsion systems: an approach based on discontinuous finite elements*. (Cit. on pp. 8, 27, 30.)
- Richardson, Lewis F.  
1922 *Weather prediction by numerical process*, Cambridge University Press. (Cit. on p. 9.)
- Kolmogorov, Andrey Nikolaevich  
1941 ‘The local structure of turbulence in incompressible viscous fluid for very large Reynolds numbers’, *Cr Acad. Sci. URSS*, 30, pp. 301-305. (Cit. on pp. 9, 10.)

Leonard, Athony

- 1975 ‘Energy cascade in large-eddy simulations of turbulent fluid flows’, in *Advances in geophysics*, Elsevier, vol. 18, pp. 237-248. (Cit. on pp. [9](#), [15](#), [16](#).)

Kalmár-Nagy, Tamás and Bendegúz Dezső Bak

- 2019 ‘An intriguing analogy of Kolmogorov’s scaling law in a hierarchical mass–spring–damper model’, *Nonlinear Dynamics*, 95, 4, pp. 3193-3203. (Cit. on p. [12](#).)

Stoll, Rob

- 2014 *LES of Turbulent Flows: Lecture 4*. (Cit. on p. [18](#).)

Laval, Jean-Philippe

- 2020 *Lecture Notes on DNS and LES for International Masters Program in Turbulence*. (Cit. on p. [19](#).)

Maulik, Romit and Omer San

- 2018 ‘Explicit and implicit LES closures for Burgers turbulence’, *Journal of Computational and Applied Mathematics*, 327, pp. 12-40. (Cit. on p. [23](#).)

Boussinesq, Joseph

- 1877 *Essai sur la théorie des eaux courantes*, Impr. nationale. (Cit. on p. [24](#).)

Germano, Massimo, Ugo Piomelli, Parviz Moin, and William H Cabot

- 1991 ‘A dynamic subgrid-scale eddy viscosity model’, *Physics of Fluids A: Fluid Dynamics*, 3, 7, pp. 1760-1765. (Cit. on p. [24](#).)

Lilly, Douglas K

- 1992 ‘A proposed modification of the Germano subgrid-scale closure method’, *Physics of Fluids A: Fluid Dynamics*, 4, 3, pp. 633-635. (Cit. on p. [24](#).)

Lund, TS

- 2003 ‘The use of explicit filters in large eddy simulation’, *Computers & Mathematics with Applications*, 46, 4, pp. 603-616. (Cit. on p. [25](#).)

Reed, William H and TR Hill

- 1973 *Triangular mesh methods for the neutron transport equation*, tech. rep., Los Alamos Scientific Lab., N. Mex.(USA). (Cit. on p. [27](#).)

Bassi, Francesco, Lorenzo Botti, Alessandro Colombo, Daniele A Di Pietro, and Pietro Tesini

- 2012 ‘On the flexibility of agglomeration based physical space discontinuous Galerkin discretizations’, *Journal of Computational Physics*, 231, 1, pp. 45-65. (Cit. on p. [30](#).)

Osher, Stanley and Fred Solomon

- 1982 ‘Upwind difference schemes for hyperbolic systems of conservation laws’, *Mathematics of computation*, 38, 158, pp. 339-374. (Cit. on p. 30.)

Pandolfi, Maurizio

- 1984 ‘A contribution to the numerical prediction of unsteady flows’, *AIAA journal*, 22, 5, pp. 602-610. (Cit. on p. 30.)

Gassner, Gregor and David A Kopriva

- 2011 ‘A comparison of the dispersion and dissipation errors of Gauss and Gauss–Lobatto discontinuous Galerkin spectral element methods’, *SIAM Journal on Scientific Computing*, 33, 5, pp. 2560-2579. (Cit. on pp. 30, 31.)

Beck, Andrea D, Thomas Bolemann, David Flad, Hannes Frank, Gregor J Gassner, Florian Hindenlang, and Claus-Dieter Munz

- 2014 ‘High-order discontinuous Galerkin spectral element methods for transitional and turbulent flow simulations’, *International Journal for Numerical Methods in Fluids*, 76, 8, pp. 522-548. (Cit. on p. 31.)

Stadtmüller, Peter, Leonhard Fottner, and Andreas Fiala

- 2000 ‘Experimental and numerical investigation of wake-induced transition on a highly loaded LP turbine at low Reynolds numbers’, in *Turbo Expo: Power for Land, Sea, and Air*, American Society of Mechanical Engineers, vol. 78569, V003T01A074. (Cit. on pp. 32-34, 39, 42, 47, 48.)

Wissink, JG

- 2003 ‘DNS of separating, low Reynolds number flow in a turbine cascade with incoming wakes’, *International Journal of Heat and Fluid Flow*, 24, 4, pp. 626-635. (Cit. on p. 33.)

Sandberg, RD, R Pichler, and L Chen

- 2012 ‘Assessing the sensitivity of turbine cascade flow to inflow disturbances using direct numerical simulation’. (Cit. on pp. 33, 34.)

Michelassi, Vittorio, Li-Wei Chen, Richard Pichler, and Richard D Sandberg

- 2015 ‘Compressible Direct Numerical Simulation of Low-Pressure Turbines—Part II: Effect of Inflow Disturbances’, *Journal of Turbomachinery*, 137, 7. (Cit. on p. 33.)

Dubief, Yves and Franck Delcayre

- 2000 ‘On coherent-vortex identification in turbulence’, *Journal of turbulence*, 1, 1, pp. 011-011. (Cit. on p. 45.)

Sagaut, Pierre

- 2006 *Large eddy simulation for incompressible flows: an introduction*, Springer Science & Business Media.

Lax, Peter D

- 1954 'Weak solutions of nonlinear hyperbolic equations and their numerical computation', *Communications on pure and applied mathematics*, 7, 1, pp. 159-193.

# List of Abbreviations

<b>ADM</b>	Approximate Deconvolution Method
<b>CFD</b>	Computational Fluid Dynamics
<b>DES</b>	Detached-Eddy Simulation
<b>DIMEAS</b>	Department of Mechanical and Aerospace Engineering
<b>DNS</b>	Direct Numerical Simulation
<b>ESR</b>	Enhanced Stability Recovery
<b>FSTI</b>	Free-Stream Turbulence Intensity
<b>ILES</b>	Implicit Large-Eddy Simulation
<b>LE</b>	Leading Edge
<b>LES</b>	Large-Eddy Simulation
<b>LPT</b>	Low Pressure Turbine
<b>RANS</b>	Reynolds-Averaged Navier-Stokes
<b>RSM</b>	Reynolds Stress Model
<b>SAS</b>	Scale-Adaptive Simulation
<b>SGS</b>	Sub-Grid Scale
<b>TE</b>	Trailing Edge